Towards gigantic RVE sizes for 3D stochastic fibrous networks

J. Dirrenberger [a,b,*], S. Forest [a], D. Jeulin [a,b]

[a] Centre des Matériaux, MINES-ParisTech, CNRS UMR 7633, BP 87, 91 003 Evry Cedex, France
[b] Centre de Morphologie Mathématique, MINES-ParisTech, 35, rue St-Honoré, 77 305 Fontainebleau, France

ABSTRACT

The size of representative volume element (RVE) for 3D stochastic fibrous media is investigated. A statistical RVE size determination method is applied to a specific model of random microstructure: Poisson fibers. The definition of RVE size is related to the concept of integral range. What happens in microstructures exhibiting an infinite integral range? Computational homogenization for thermal and elastic properties is performed through finite elements, over hundreds of realizations of the stochastic microstructural model, using uniform and mixed boundary conditions. The generated data undergoes statistical treatment, from which gigantic RVE sizes emerge. The method used for determining RVE sizes was found to be operational, even for pathological media, i.e., with infinite integral range, interconnected percolating porous phase and infinite contrast of properties.

© 2013 Elsevier Ltd. All rights reserved.

1. Introduction

Microstructural heterogeneities play a critical role on the macroscopic physical properties of materials. One common way to account for this underlying complexity is resorting to homogenization techniques. Many approaches, including analytical and computational ones, are available for determining the homogenized properties of random media. Most of them necessitate the existence of a representative volume element (RVE). Several definitions have been given for the RVE over the past 50 years. A review of this topic can be found in Gitman et al. (2007).

The classical definition of RVE is attributed to Hill (1963), who stated that for a given material the RVE is a sample that is structurally typical of the whole microstructure, i.e., containing a sufficient number of heterogeneities for the macroscopic properties to be independent of the boundary values of traction and displacement. Later, Beran (1968) emphasized the role of statistical homogeneity, especially in a volume-averaged sense. This also means that the RVE size considered should be larger than a certain microstructural length for which moduli fluctuate. Hashin (1983) made a review on analysis of composite materials in which he referred to statistical homogeneity as a practical necessity. Sab (1992) considered that the classical RVE definition for a heterogeneous medium holds only if the homogenized properties tend towards those of a similar periodic medium. This entails that the response over an RVE should be independent of boundary conditions (BC). From numerical simulations on VEs of various sizes, Terada et al. (2000) concluded that from a practical viewpoint RVE should be as large as possible. Ostoja-Starzewski (2002) considers the RVE to be only defined over a periodic unit-cell or a non-periodic cell containing an infinite number of heterogeneities. Drugan and Willis (1996) introduced explicitly the idea of minimizing the RVE size, meaning that the RVE would be the smallest material volume for which the apparent and effective properties coincide. It is worth noticing that for a given material the RVE size for thermal properties is a priori different from the RVE size for elastic properties. Thus, one has to consider an RVE that depends on the specific investigated property.

Taking into account these definitions, and assuming ergodicity for the heterogeneous media considered, Kanit et al. (2003) proposed a method based on a statistical analysis for computing the minimal RVE size for a given physical property Z and precision in the estimate of effective properties. The computed RVE size was found to be proportional to the integral range (Matheron, 1971), which corresponds to a volume of statistical correlation.

This approach was implemented in many papers, such as Pelissou et al. (2009) and Jean et al. (2011). In these papers, the authors resorted to periodic boundary conditions (PBC) since Kanit et al. (2003) showed from computational experiments that mean apparent properties obtained with PBC converge faster towards the effective properties than with the Dirichlet and Neumann-type BC. Nevertheless, the Dirichlet and Neumann-type BC can be useful for bounding the effective properties of heterogeneous media. If the microstructure features a matrix phase, tighter bounds can be obtained by choosing elementary volumes including only the matrix at the boundary, as shown in Salmi et al. (2012). Furthermore, the rate of convergence of the mean value for apparent properties, with respect to the size of the system, is related to the size of the statistical RVE. For example, a microstructure with slow rate of convergence would yield large RVE sizes.

Computational techniques using finite elements (FE) are available for homogenizing percolating porous materials, given a proper BC treatment in order to deal with voids at the boundary of the RVE. Therefore, the statistical method of Kanit et al. (2003) for determining RVE sizes could be used in this context.

Furthermore, some porous materials may exhibit an infinite integral range for some geometrical or physical property, due to very long range of correlations. The fact that RVE size is directly related to the integral range suggests that such "pathological" microstructures can lead to gigantic RVE sizes, or even no RVE at all, i.e., yield non-homogenizability in the sense of Auriault (1991). For instance, it could be the case for a tridimensional stochastic network made of infinitely long fibers. Although infinite fibers do not exist in nature, they can be considered a limit case representative of sintered long-fiber non-woven materials, such as those studied by Mezeix et al. (2009).

Many studies are available regarding finite-length fibrous media and strongly oriented infinite-fiber media. For instance, Delisée et al. (2001) and Peyrega et al. (2009) dealt with the morphology of 3D long fibers randomly oriented in-plane, Schladitz et al. (2006) used a 3D random model of randomly oriented long-fibers for the design of an acoustic absorber, and Barbier et al. (2009b,a) generated virtual samples of long but finite fibers for modeling the mechanics of entangled materials. None of these studies accounted for the representativity of samples. Oumarou et al. (2012) computed RVE sizes for 2D random arrays of fibers, using the statistical method of Kanit et al. (2003). The works of Soare and Picu (2007), Hatami-Marbini and Picu (2009), Picu and Hatami-Marbini (2010), Picu (2011) on 2D fibrous fractal networks also deal with the representativity and homogenization of such, yet self-similar, fibrous media. Recently, Shahsavari and Picu (2013) dealt with the size effect on mechanical behavior for 2D random fiber networks, and showed that RVE size depends on fiber properties and density.

To the knowledge of the authors, no one ever assessed the question of RVE size for 3D infinite randomly oriented fibrous media, or for porous random media with infinite integral range. This is the main goal of this study, as well as testing the approach of Kanit et al. (2003) for a pathological model of random structure: Poisson fibers.

This model corresponds to a 3D stochastic network composed by randomly oriented and distributed infinitely-long interpenetrating rectilinear fibers. It exhibits an infinite integral range (Jeulin, 1991), i.e., an infinite morphological correlation length; this medium is non-periodizable without modifying its morphology, thus falling beyond the spectrum of periodic homogenization and the definition of RVE proposed by Sab (2005).

In this paper, a computational homogenization scheme is implemented based on FE simulations. This requires virtual samples generated using a specific mathematical morphology model, which is described in Jeulin (2012) along with a review on the determination of effective properties for random sets, including Poisson fibers.

First, the microstructural model is described in Section 2 along with the virtual samples generation procedure and computational strategy. The porous and stochastic nature of the microstructures considered here requires a specific treatment of the thermal and elastic boundary value problems, this is done in Section 3. Results coming from the FE simulations are presented in Section 4. The discussion of these results and their consequences on the RVE size is postponed to Section 5.

Throughout this work, the following notation is used: x for scalars, $\underline{x}$ for vectors, $\mathbf{x}$ for 2nd-order tensors, $\underset{\approx}{\mathbf{x}}$ for 4th-order tensors, $\cdot$ for dot product, $:$ for doubly-contracted dot product, $\otimes$ for tensor product, $\overset{s}{\otimes}$ for symmetric tensor product, $\oplus$ for dilation by a compact set, $\langle x \rangle$ for spatial average and $\bar{x}$ for ensemble average.

2. Microstructural model

Based on morphological arguments, a specific model of random structures is defined: Poisson fibers. This microstructural model is made of a Boolean model on a Poisson linear variety, and was explicited in Jeulin (1991, 2011, 2012). The different notions used for designing the model are recalled briefly hereafter.

2.1. Morphological description

The Poisson point process is a random point process on which many stochastic models are based, see for instance (Serra, 1982); it is the prototype for random processes without any order. It consists in implanting points x_i in $\mathbb{R}^n$ according to a Poisson law (Poisson, 1837) with intensity θ, namely the average number of Poisson points per unit volume. For instance, $P(m)$ is the probability for m Poisson points to be implanted with intensity θ in a two-dimensional domain with surface area S:

$$P(m) = \frac{(\theta S)^m}{m!} \exp(-\theta S) \tag{1}$$

Let us now consider a Poisson point process $\{x_i(\omega)\}$, with intensity $\theta_k(d\omega)$ on the variety of dimension $(n-k)$ containing the origin O, and with orientation ω. For every point $x_i(\omega)$ there is a variety of dimension k, called $V_k(\omega)_{x_i}$, that is orthogonal to the direction ω. Let us consider the set V_k, which is the union over $\{x_i(\omega)\}$ of all varieties, such that:

$$V_k = \cup_{x_i(\omega)} V_k(\omega)_{x_i} \tag{2}$$

Using this definition in $\mathbb{R}^3$, one can for instance generate a network of Poisson hyperplanes ($k = 2$) or Poisson lines ($k = 1$).

The number of varieties of dimension k hit by a compact set K is a Poisson variable with parameter $\theta(K)$, and as proved in Jeulin (1991) for the stationary case:

$$\theta(K) = \int_{4\pi \text{ster}} \theta_k(d\omega) \mu_{n-k}(K(\omega)) \tag{3}$$

where μ_{n-k} is the Lebesgue measure on $\mathbb{R}^{n-k}$ and $K(\omega)$ is the orthogonal projection of K on the space orthogonal to $V_k(\omega), V_{k\perp}(\omega)$.

In the isotropic (θ_k being constant) stationary case of Poisson lines in $\mathbb{R}^3$ ($n = 3, k = 1$), for a convex set K, it can be proved (Jeulin, 1991) that the number of varieties of dimension k hit by a compact set K is a Poisson variable, with parameter $\theta(K)$:

$$\theta(K) = \frac{\pi}{4} \theta \mathcal{S}(K) \tag{4}$$

where $\mathcal{S}$ is the measure of surface area in $\mathbb{R}^3$.

Boolean random sets can be built from Poisson varieties and a primary grain A', as described in Jeulin (1991, 2011). A Boolean

model built on Poisson lines generates a fibrous network, with a possible overlap of fibers. According to Jeulin (1991), the Choquet capacity, i.e., the probability for the intersection between the set A and the compact set K not be empty, of a Boolean random model built on a Poisson variety of dimension k reads as:

$$T(K) = 1 - \exp\left(-\int_{4\pi\text{ster}} \theta_k(d\omega)\overline{\mu}_{n-k}(A'(\omega) \oplus \check{K}(\omega))\right) \qquad (5)$$

In the case of isotropic Poisson lines, for a convex set $A' \oplus \check{K}$, the Choquet capacity simplifies to:

$$T(K) = 1 - \exp\left(-\theta\frac{\pi}{4}\bar{\mathcal{S}}(A' \oplus \check{K})\right) \qquad (6)$$

Thus, for Poisson fibers resulting from the dilation of isotropic Poisson lines by a sphere of radius R:

$$T(0) = P\{x \in A\} = 1 - \exp(-\theta\pi^2 R^2) \qquad (7)$$

For a given volume fraction V_V^f of Poisson fibers, θ is obtained as follows:

$$\theta = \frac{-\ln(1 - V_V^f)}{\pi^2 R^2} \qquad (8)$$

Based on Eq. (8), one can compute the average number of Poisson fibers $\bar{N}$ for a given set of parameters in the model: the fiber radius R, the volume fraction of fibers V_V^f and the considered cubic volume $V = L^3$:

$$\bar{N} = \frac{\pi}{4}S\theta = \frac{\pi}{4}6L^2 \frac{-\ln\left(1 - V_V^f\right)}{\pi^2 R^2} = \frac{-3\ln\left(1 - V_V^f\right)}{2\pi}\frac{L^2}{R^2} \qquad (9)$$

with $\frac{L^2}{R^2}$ ratio of characteristic lengths, and $S = 6L^2$ the surface area of the cube in $\mathbb{R}^3$.

2.2. Generation of Poisson fibers virtual models

Based on the aforementioned definition of Poisson fibers, virtual models or realizations can be generated. In this work we relied on `vtkSim`[1] (Faessel and Jeulin, 2011). This software is able to generate tridimensional random structures based on a morphological description. It is programmed in C++ and based on the `vtk`[2] graphics library (Schroeder et al., 2006). This software operates on a vectorial framework making the computation time for generating random structures almost size-independent until discretization. This allows one to generate very large random structures with a good spatial precision, in comparison with voxel-based software.

The algorithm developed for generating Poisson fibers is given hereafter and illustrated in Fig. 1.

1. Input: volume fraction of isotropic fibers V_V^f, fiber radius R, sample size L ($V = L^3$).
2. Compute the theoretical average number of germs for implanting fibers $n_{\text{theo}} = \frac{-3L^2 \ln(1-V_V^f)}{2\pi R^2}$.
3. Monte-Carlo simulation for determining the number of germs n_{simul} according to a Poisson law.
4. Generate and implant the nth Poisson line.
   - Randomize angles ρ and ϕ accounting for the fiber orientation.
   - Rotate the equatorial plan $\Pi \to \Pi' \to \Gamma$ after angles ρ and ϕ.
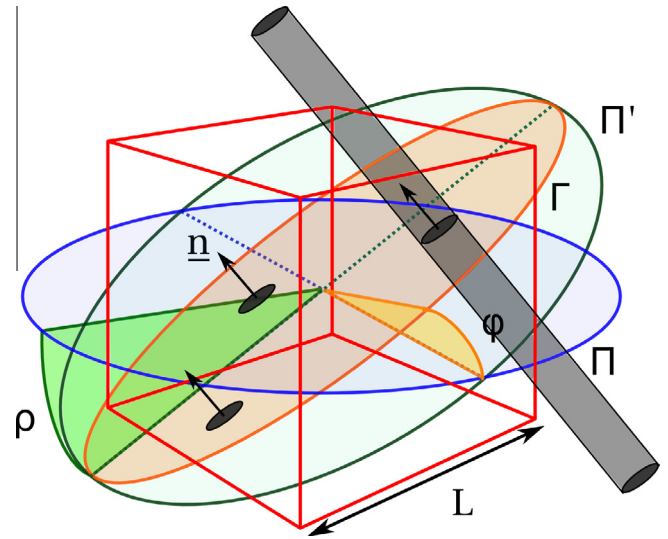

Fig. 1. Geometrical model for generating Poisson fibers.

   - Randomize coordinates $\{x, y\}$ of the germ on the disc Γ and trace the normal of Γ in $\{x, y\}$.
5. Repeat Step 4 while $n \le n_{\text{simul}}$.
6. Dilate the ensemble of Poisson lines by the sphere of radius R.
7. Write geometric data file.

2.3. Discretization and parameters for simulation

The generated realizations are then discretized for further use with FE. `vtkSim` uses the meshing tools of the `vtk` library, which provides 3D regular triangular meshes attached to a Cartesian grid. The spacing of the grid is inversely proportional to the mesh density. These meshes cannot be used directly for FE computations for two reasons: they are only 3D surface meshes; they are not optimized. In order to obtain a 3D volume mesh based on a 3D closed surface mesh, the latter is filled with tetrahedra. This was done using the Z-Set FE package[3] interfaced with the meshing tools developed at INRIA[4]. This procedure first consists in a shape optimization of the 3D surface mesh using `YAMS` software (Frey, 0252). The resulting closed surface mesh is then filled with `TetMesh–GHS3D` software (SIMULOG, 2003) using a Voronoi–Delaunay algorithm. The volumic meshes obtained are suitable for computational homogenization through FE. The shape of the generated samples is chosen cubic for simplicity of computational implementation; an alternative could have been spherically-shaped samples as developed in Glüge et al. (2012), in which the authors have found that spherical volume elements lead to a faster convergence of the effective properties in contrast to cubic volumes. However, no difference is expected at convergence for the RVE size, i.e., the value of the scaling-law exponent γ for the ensemble variance of a given physical property, which is asymptotically obtained for any shape of the volume elements.

There are several parameters to be set for the simulation, summarized in Table 1. Volume fraction V_V of fibers was chosen to be 16%. This arbitrary value is large enough to obtain an interconnected percolating medium, and small enough to compute large volumes. Fibre radius R is kept constant and equal to 1 as a convention, hence setting the unit-length for the computation of elementary volumes. Different simulation sizes L are considered. It corresponds to the edge length of the simulation cube of volume $V = L^3$. This length ranges from 10 to 100. Examples of virtual sam-

---

Table 1
Simulation parameters for estimating effective properties.

Simulation size (L)	Fiber radius	Volume fraction
[10; 100]	1	0.16

ple realizations are shown for different sizes on Fig. 2. The effect of mesh density was investigated for 4 different values of geometrical discretization. The smallest mesh density yielding converged results, in terms of morphology and elastic properties, was chosen and kept constant for further computations; this corresponds to Fig. 3(b), which gives a statisfactory geometrical description of the model for a relatively low number of elements, allowing us to consider more fibers in the simulation.

2.4. Validation of the numerical model

In order to check that the numerically generated models correspond to the theoretical morphological model, morphological isotropy was investigated on a sample of volume 60^3, with approximately $\bar{N} = 285$ fibers, as shown on Fig. 4.

This virtual sample was sliced and voxelized. Its covariance was estimated on different slices. The morphological covariance $C(\underline{x}, \underline{x} + \underline{h})$ of a random set A is given by:

$$C(\underline{x}, \underline{x} + \underline{h}) = P\{\underline{x} \in A, \underline{x} + \underline{h} \in A\} \tag{10}$$

Results were averaged over all the slices, and are plotted on Fig. 5. For 4 different orientations ω of the vector $\underline{h}$, the covariance reaches its sill for a separation close to 2 pixels, which corresponds to the diameter of one fiber. One would expect the covariance to converge for longer correlation lengths in the case of Poisson fibers. This is true for an infinite medium. In the case of a limited sample like this one, the probability for fibers to be aligned with $\underline{h}$ is very small. Anyway, the value of convergence does not depend on the orientation ω. From a morphological viewpoint, this thus verifies isotropy of the generated models. A second verification is performed in Section 5.1 regarding homogenized properties.

2.5. Computational strategy

Since a vectorial framework was used for generating samples, binarization was avoided in order to keep the number of degrees of freedom (DOFs) low for a given morphological description. Voxel-based computational homogenization methods were put aside, such as Fast-Fourier Transform-based (FFT) (Moulinec et al., 1994) and FE with multi-phase elements (Barbe et al., 2001). We opted for volumic FE with free meshes using linear tetrahedra for efficiency. Sequential computations were considered for the sake of simplicity. The FE package Z-Set 8.5 was used for the computation as it is developed in-house and has previously been used with success for computing properties of heterogeneous microstructures as in Cailletaud et al. (2003), Madi et al. (2005), Jean et al. (2011), Dirrenberger et al. (2012), Dirrenberger et al. (2013).

The many simulations considered in this work were performed on the computing cluster of the Centre des Matériaux, allowing us to run many sequential computations in a parallel manner. The largest computation considered in this paper corresponds to a
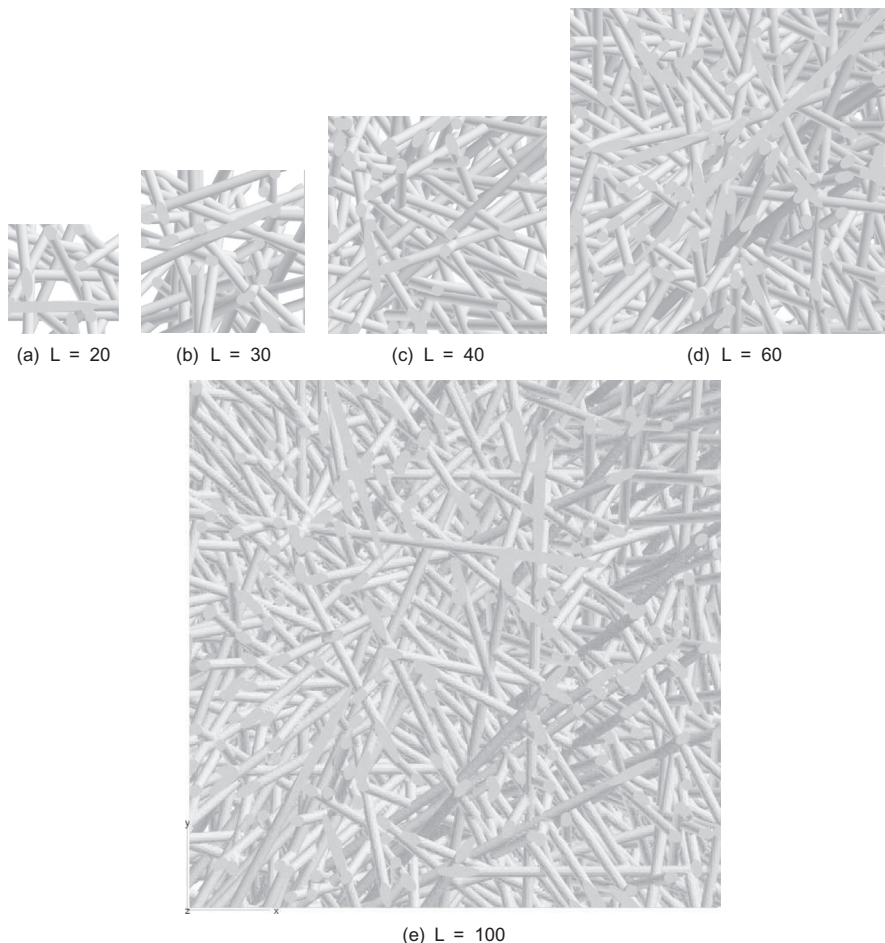
Fig. 2. 3D rendering of Poisson fibers models (a) $L = 20$, (b) $L = 30$, (c) $L = 40$, (d) $L = 60$ and (e) $L = 100$.
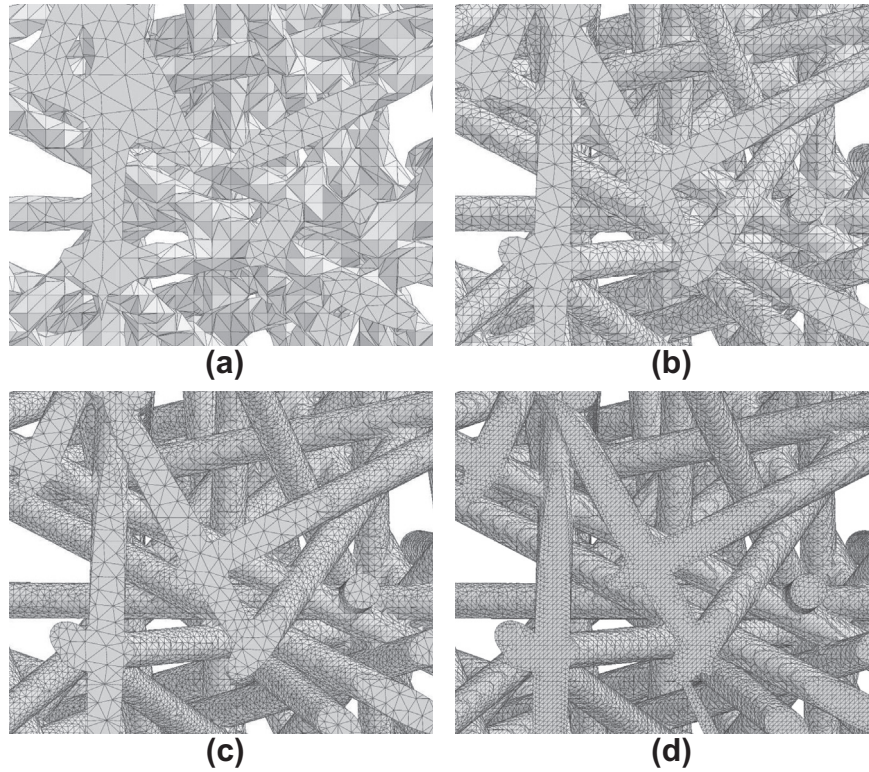
(a) L = 20   (b) L = 30   (c) L = 40   (d) L = 60

(e) L = 100

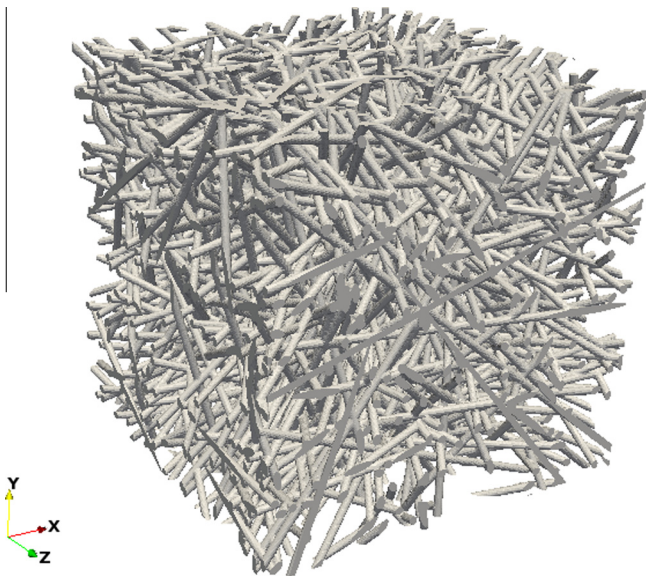**Fig. 3.** Mesh descretization: (a) coarse, (b) standard, (c) fine and (d) finer.

Fig. 4. Elementary volume of fibers on which the covariance is computed ($L = 60$).

Fig. 5. Covariance of the Poisson fibers determined on 2D slices for several orientations ω.

volume $V = 10^6$ including ca. 800 Poisson fibers. The associated mesh includes 11 million linear tetrahedral elements, i.e., 7.6 million DOFs. The `MUMPS` linear solver (Amestoy et al., 2000) was used as it was the most efficient available. For comparison, about 128 GB of RAM were necessary for the whole resolution of a linear elastic problem with the largest mesh using the default `DSCPACK` linear solver (Raghavan, 2002), whereas `MUMPS` only needed 54 GB. Timewise, the computation itself takes about 2.5 h for an elastic problem on a AMD Opteron 6134 single-core @ 2.3 GHz, while the post-processing takes another half hour. All the data considered in this paper was generated over a duration of 4 months computation time; this does not include meshing.

3. Boundary value problems and averaging relations

Using the microstructural model defined in Section 2, the apparent thermal and elastic properties are computed through FE simulations. After discussing and adapting the averaging relations for the thermal and mechanical fields to the case of Poisson fibers, the boundary value problems considered in the simulations will be explicited.

As shown on Fig. 6, the elementary volume considered in the computation is the volume V that is composed of two complementary phases V_f and V_p, respectively accounting for the Poisson fibers and the porous phase, such that:

Fig. 6. Example of an elementary volume of Poisson fibers used in the simulation.

$$V = V_f \cup V_p \tag{11}$$

Let us consider the boundary of each phase:

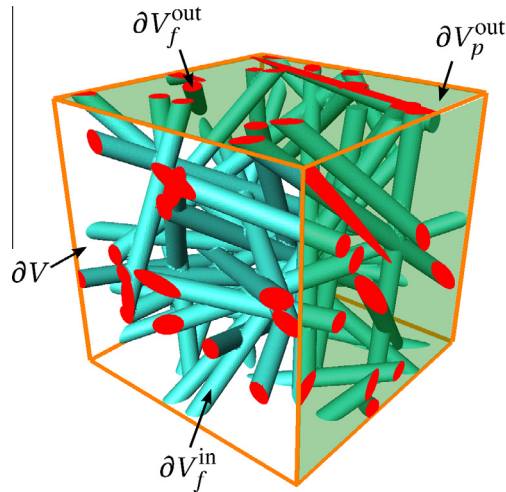$$\partial V_f = \partial V_f^{\text{in}} \cup \partial V_f^{\text{out}} \tag{12}$$

$$\partial V_p = \partial V_p^{\text{in}} \cup \partial V_p^{\text{out}} \tag{13}$$

with exponent $^{\text{in}}$ and $^{\text{out}}$, respectively accounting for the internal and external boundaries of the phases. For instance, $\partial V_f^{\text{out}}$ corresponds to the set of red surfaces in Fig. 6. Moreover, for the normal vector $\underline{\boldsymbol{n}}$:

$$\underline{\boldsymbol{n}}_f^{\text{in}} = -\underline{\boldsymbol{n}}_p^{\text{in}} \quad \forall \underline{\boldsymbol{x}} \in \partial V_{f,p}^{\text{in}} \tag{14}$$

with $\underline{\boldsymbol{x}}$ being the material point vector.

Finally, the boundary ∂V of the elementary volume considered is made of the 6 faces of the cube $F_1^+, F_1^-, F_2^+, F_2^-, F_3^+$ and F_3^-. ∂V can also be defined as the union of the external boundaries of each phase:

$$\partial V = \partial V_f^{\text{out}} \cup \partial V_p^{\text{out}} \tag{15}$$

For the linear steady-state thermal conduction case, the following field equation must be satisfied:

$$\text{Div}\,\underline{\boldsymbol{q}} = 0 \quad \forall \underline{\boldsymbol{x}} \in V_f \tag{16}$$

in the absence of heat source.

The temperature T and heat flux $\underline{\boldsymbol{q}}$ fields are defined on the elementary volume V: they are computed on V_f only; on V_p, fields T and $\underline{\boldsymbol{q}}$ may be considered as extensions of T and $\underline{\boldsymbol{q}}$ on V_f using suitable interpolations assuming continuity for T and $\underline{\boldsymbol{q}} \cdot \underline{\boldsymbol{n}}$ on $\partial V_{f,p}^{\text{in}}$. We adopt the following extension of the $\underline{\boldsymbol{q}}$ field on V_p:

$$\underline{\boldsymbol{q}}(\underline{\boldsymbol{x}}) = \underline{\boldsymbol{0}} \quad \forall \underline{\boldsymbol{x}} \in V_p \tag{17}$$

This choice is compatible with the condition,

$$\underline{\boldsymbol{q}}(\underline{\boldsymbol{x}}) \cdot \underline{\boldsymbol{n}} = 0 \quad \forall \underline{\boldsymbol{x}} \in \partial V_f^{\text{in}} \tag{18}$$

For the linear elastic static case, the following field equation must be satisfied:

$$\text{Div}\,\underset{\sim}{\boldsymbol{\sigma}} = \underline{\boldsymbol{0}} \quad \forall \underline{\boldsymbol{x}} \in V_f \tag{19}$$

in the absence of body forces.

The displacement $\underline{\boldsymbol{u}}$ and stress $\underset{\sim}{\boldsymbol{\sigma}}$ fields are defined on the elementary volume V as well: they are computed on V_f only. Over V_p, the fields $\underline{\boldsymbol{u}}$ and $\underset{\sim}{\boldsymbol{\sigma}}$ may be considered as extensions of $\underline{\boldsymbol{u}}$ and $\underset{\sim}{\boldsymbol{\sigma}}$ on V_f using suitable interpolations assuming continuity for $\underline{\boldsymbol{u}}$ and $\underset{\sim}{\boldsymbol{\sigma}} \cdot \underline{\boldsymbol{n}}$ on $\partial V_{f,p}^{\text{in}}$. We adopt the following extension of the $\underset{\sim}{\boldsymbol{\sigma}}$ field on V_p:

$$\underset{\sim}{\boldsymbol{\sigma}}(\underline{\boldsymbol{x}}) = \underline{\boldsymbol{0}} \quad \forall \underline{\boldsymbol{x}} \in V_p \tag{20}$$

This choice is compatible with the condition of free internal surfaces of the fibers:

$$\underset{\sim}{\boldsymbol{\sigma}}(\underline{\boldsymbol{x}}) \cdot \underline{\boldsymbol{n}} = \underline{\boldsymbol{0}} \quad \forall \underline{\boldsymbol{x}} \in \partial V_f^{\text{in}} \tag{21}$$

For both thermal and mechanical problems, the choices of interpolation made are compatible with the condition of fibers free boundaries used in the computation.

For determining the apparent thermal and elastic properties of Poisson fibers, we consider first the classical Dirichlet- and Neumann-type boundary conditions, also known respectively as kinematic uniform boundary conditions (KUBC) and static uniform boundary conditions (SUBC) in mechanics, and uniform temperature gradient boundary conditions (UTG) and uniform heat flux boundary conditions (UHF) in the thermal case. We consider also new mixed boundary conditions, that will be presented hereafter for the elastic and thermal problems.

3.1. Averaging relations for thermal fields

The averaging equations for ∇T and $\underline{\boldsymbol{q}}$ are recalled and adapted hereafter for the homogenization of porous media. If one considers the spatial average over V of the gradient of temperature ∇T:

$$\begin{aligned}
\langle \nabla T \rangle &= \frac{1}{V} \int_V \nabla T dV = \frac{1}{V} \int_{V_f} \nabla T dV + \frac{1}{V} \int_{V_p} \nabla T dV \\
&= \frac{1}{V} \int_{\partial V_f} T\underline{\boldsymbol{n}}\, dS + \frac{1}{V} \int_{\partial V_p} T\underline{\boldsymbol{n}}\, dS \\
&= \frac{1}{V} \int_{\partial V_f^{\text{out}}} T\underline{\boldsymbol{n}}\, dS + \frac{1}{V} \int_{\partial V_p^{\text{out}}} T\underline{\boldsymbol{n}}\, dS
\end{aligned} \tag{22}$$

The value of $\langle \nabla T \rangle$ therefore depends on the interpolation chosen for T on $\partial V_p^{\text{out}}$.

If one considers now the spatial average over V of a steady-state heat flux vector $\underline{\boldsymbol{q}}^*$, i.e., $\text{Div}\underline{\boldsymbol{q}}^* = 0$ in V, it yields:

$$\begin{aligned}
\langle \underline{\boldsymbol{q}}^* \rangle &= \frac{1}{V} \int_{V_f} \underline{\boldsymbol{q}}^* dV + \underbrace{\frac{1}{V} \int_{V_p} \underline{\boldsymbol{q}}^* dV}_{=0 \text{ cf. Eq. (17)}} \\
&= \frac{1}{V} \int_{\partial V_f^{\text{out}}} \left(\underline{\boldsymbol{q}}^* \cdot \underline{\boldsymbol{n}} \right) \underline{\boldsymbol{x}}\, dS + \underbrace{\frac{1}{V} \int_{\partial V_f^{\text{in}}} \left(\underline{\boldsymbol{q}}^* \cdot \underline{\boldsymbol{n}} \right) \underline{\boldsymbol{x}}\, dS}_{=0 \text{ cf. Eq. (18)}} \\
&= \frac{1}{V} \int_{\partial V_f^{\text{out}}} \left(\underline{\boldsymbol{q}}^* \cdot \underline{\boldsymbol{n}} \right) \underline{\boldsymbol{x}}\, dS
\end{aligned} \tag{23}$$

From a practical viewpoint, $\langle \underline{\boldsymbol{q}} \rangle$ is computed on the fibers in this way:

$$\langle \underline{\boldsymbol{q}} \rangle = \frac{1}{V} \int_{V_f} \underline{\boldsymbol{q}}\, dV = \frac{V_f}{V} \frac{1}{V_f} \int_{V_f} \underline{\boldsymbol{q}}\, dV = V_V^f \langle \underline{\boldsymbol{q}} \rangle_f \tag{24}$$

Finally, let us consider the thermal dissipation rate density $\mathcal{D}$th that arises from the fields $\underline{\boldsymbol{q}}^*$ and ∇T in the porous linear case for a reference temperature T_0 (linearized theory):

$$T_0 \mathcal{D}\text{th} = \langle -\boldsymbol{q}^* \cdot \nabla T \rangle = \frac{1}{V} \int_{V_f} -\boldsymbol{q}^* \cdot \nabla T dV$$

$$= \frac{1}{V} \int_{\partial V_f^{\text{out}}} -T\boldsymbol{q}^* \cdot \underline{\boldsymbol{n}} dS + \underbrace{\frac{1}{V} \int_{\partial V_f^{\text{in}}} -T\boldsymbol{q}^* \cdot \underline{\boldsymbol{n}} dS}_{=0 \text{ cf. Eq. (18)}}$$

$$= \frac{1}{V} \int_{\partial V_f^{\text{out}}} -T\boldsymbol{q}^* \cdot \underline{\boldsymbol{n}} dS \qquad (25)$$

In practice, $T_0 \mathcal{D}\text{th}$ is computed this way:

$$T_0 \mathcal{D}\text{th} = \langle -\boldsymbol{q} \cdot \nabla T \rangle = \frac{1}{V} \int_{V_f} -\boldsymbol{q} \cdot \nabla T dV \qquad (26)$$

3.2. Averaging relations for mechanical fields

The averaging relations for the strain $\underset{\sim}{\varepsilon}$ and stress $\underset{\sim}{\sigma}$ fields are recalled and adapted for the homogenization of porous media. Let us consider the spatial average over V of the kinematically compatible strain field $\underset{\sim}{\varepsilon}'$, which is defined as the symmetric part of the gradient of the displacement field $\underline{\boldsymbol{u}}'$:

$$\langle \underset{\sim}{\varepsilon}' \rangle = \frac{1}{V} \int_V \underset{\sim}{\varepsilon}' dV = \frac{1}{V} \int_{V_f} \underset{\sim}{\varepsilon}' dV + \frac{1}{V} \int_{V_p} \underset{\sim}{\varepsilon}' dV$$

$$= \frac{1}{V} \int_{\partial V_f} \underline{\boldsymbol{u}}' \overset{s}{\otimes} \underline{\boldsymbol{n}} dS + \frac{1}{V} \int_{\partial V_p} \underline{\boldsymbol{u}}' \overset{s}{\otimes} \underline{\boldsymbol{n}} dS$$

$$= \frac{1}{V} \int_{\partial V_f^{\text{out}}} \underline{\boldsymbol{u}}' \overset{s}{\otimes} \underline{\boldsymbol{n}} dS + \frac{1}{V} \int_{\partial V_p^{\text{out}}} \underline{\boldsymbol{u}}' \overset{s}{\otimes} \underline{\boldsymbol{n}} dS \qquad (27)$$

The value of $\langle \underset{\sim}{\varepsilon}' \rangle$ depends on the interpolation chosen for $\underline{\boldsymbol{u}}'$ on $\partial V_p^{\text{out}}$. If one considers now the spatial average over V of a statically admissible stress field $\underset{\sim}{\sigma}^*$, i.e., $\text{Div}\underset{\sim}{\sigma}^* = \underline{\boldsymbol{0}}$ in V, it yields:

$$\langle \underset{\sim}{\sigma}^* \rangle = \frac{1}{V} \int_V \underset{\sim}{\sigma}^* dV = \frac{1}{V} \int_{V_f} \underset{\sim}{\sigma}^* dV + \underbrace{\frac{1}{V} \int_{V_p} \underset{\sim}{\sigma}^* dV}_{=0 \text{ cf. Eq. (20)}}$$

$$= \frac{1}{V} \int_{\partial V_f^{\text{out}}} \left(\underset{\sim}{\sigma}^* \cdot \underline{\boldsymbol{n}} \right) \overset{s}{\otimes} \underline{\boldsymbol{x}} dS + \underbrace{\frac{1}{V} \int_{\partial V_f^{\text{in}}} \left(\underset{\sim}{\sigma}^* \cdot \underline{\boldsymbol{n}} \right) \overset{s}{\otimes} \underline{\boldsymbol{x}} dS}_{=0 \text{ cf. Eq. (21)}}$$

$$= \frac{1}{V} \int_{\partial V_f^{\text{out}}} \left(\underset{\sim}{\sigma}^* \cdot \underline{\boldsymbol{n}} \right) \overset{s}{\otimes} \underline{\boldsymbol{x}} dS \qquad (28)$$

From a practical viewpoint, $\langle \underset{\sim}{\sigma} \rangle$ is computed from the fibers in this way:

$$\langle \underset{\sim}{\sigma} \rangle = \frac{1}{V} \int_{V_f} \underset{\sim}{\sigma} dV = \frac{V_f}{V} \frac{1}{V_f} \int_{V_f} \underset{\sim}{\sigma} dV = V_V^f \langle \underset{\sim}{\sigma} \rangle_f \qquad (29)$$

Finally, let us consider the elastic strain energy density $\mathcal{E}^{\text{el}}$ that arises from the fields $\underset{\sim}{\sigma}^*$ and $\underset{\sim}{\varepsilon}'$ in the porous case:

$$2\mathcal{E}^{\text{el}} = \langle \underset{\sim}{\sigma}^* : \underset{\sim}{\varepsilon}' \rangle = \frac{1}{V} \int_{V_f} \underset{\sim}{\sigma}^* : \underset{\sim}{\varepsilon}' dV$$

$$= \frac{1}{V} \int_{\partial V_f^{\text{out}}} \left(\underset{\sim}{\sigma}^* \cdot \underline{\boldsymbol{n}} \right) \cdot \underline{\boldsymbol{u}}' dS + \underbrace{\frac{1}{V} \int_{\partial V_f^{\text{in}}} \left(\underset{\sim}{\sigma}^* \cdot \underline{\boldsymbol{n}} \right) \cdot \underline{\boldsymbol{u}}' dS}_{=0 \text{ cf. Eq. (21)}}$$

$$= \frac{1}{V} \int_{\partial V_f^{\text{out}}} \left(\underset{\sim}{\sigma}^* \cdot \underline{\boldsymbol{n}} \right) \cdot \underline{\boldsymbol{u}}' dS \qquad (30)$$

Practically, $\mathcal{E}^{\text{el}}$ is computed as:

$$2\mathcal{E}^{\text{el}} = \langle \underset{\sim}{\sigma} : \underset{\sim}{\varepsilon} \rangle = \frac{1}{V} \int_{V_f} \underset{\sim}{\sigma} : \underset{\sim}{\varepsilon} dV = V_V^f \langle \underset{\sim}{\sigma} : \underset{\sim}{\varepsilon} \rangle_f \qquad (31)$$

3.3. Boundary conditions for thermal variables

3.3.1. Uniform temperature gradient boundary conditions – UTG
The macroscopic gradient of temperature $\underline{\boldsymbol{G}}$ is prescribed at the boundary of the simulation domain, such that:

$$T = \underline{\boldsymbol{G}} \cdot \underline{\boldsymbol{x}} \quad \forall \underline{\boldsymbol{x}} \in \partial V = \partial V_f^{\text{out}} \cup \partial V_p^{\text{out}} \qquad (32)$$

which yields from Eq. (22),

$$\langle \nabla T \rangle = \frac{1}{V} \int_{\partial V} (\underline{\boldsymbol{G}} \cdot \underline{\boldsymbol{x}}) \underline{\boldsymbol{n}} dS = \underline{\boldsymbol{G}} \qquad (33)$$

The macroscopic heat flux field $\underline{\boldsymbol{Q}}$ is computed in this way:

$$\underline{\boldsymbol{Q}} = \langle \boldsymbol{q} \rangle = V_V^f \langle \boldsymbol{q} \rangle_f \qquad (34)$$

3.3.2. Uniform heat flux boundary conditions – UHF
Let us now consider the case of a macroscopic heat flux $\underline{\boldsymbol{Q}} \cdot \underline{\boldsymbol{n}}$ prescribed at the boundary ∂V of the simulation domain, such that:

$$\boldsymbol{q} \cdot \underline{\boldsymbol{n}} = \underline{\boldsymbol{Q}} \cdot \underline{\boldsymbol{n}} \quad \forall \underline{\boldsymbol{x}} \in \partial V \qquad (35)$$

In the case of Poisson fibers, this condition is incompatible with the extension of the heat flux field:

$$\boldsymbol{q} = 0 \quad \forall \underline{\boldsymbol{x}} \in V_p \qquad (36)$$

so that,

$$\boldsymbol{q} \cdot \underline{\boldsymbol{n}} = 0 \quad \forall \underline{\boldsymbol{x}} \in \partial V_p \qquad (37)$$

We can only prescribe:

$$\underline{\boldsymbol{q}} \cdot \underline{\boldsymbol{n}} = \underline{\boldsymbol{Q}} \cdot \underline{\boldsymbol{n}} \quad \forall \underline{\boldsymbol{x}} \in \partial V_f^{\text{out}} \qquad (38)$$

but in the case of a random microstructure, the BC do not ensure the following balance equation:

$$\int_{\partial V} \boldsymbol{q} \cdot \underline{\boldsymbol{n}} dS = 0 \qquad (39)$$

since $\int_{\partial V_f^{\text{out}}} \boldsymbol{q} \cdot \underline{\boldsymbol{n}} dS$ does not necessarily vanish.

That is why the following alternative BC are proposed.

3.3.3. Mixed thermal boundary conditions – MTBC
Temperature is prescribed on a pair of opposite faces $F_1 = F_1^+ \cup F_1^-$ (normal to direction 1) of the boundary ∂V of the simulation domain, such that for a given uniform vector $\underline{\boldsymbol{G}}$:

$$T = \underline{\boldsymbol{G}} \cdot \underline{\boldsymbol{x}} \quad \forall \underline{\boldsymbol{x}} \in F_1 \cap \partial V_f^{\text{out}} \qquad (40)$$

The temperature field T is extended theoretically on $F_1 \cap \partial V_p^{\text{out}}$ following the same expression $T = \underline{\boldsymbol{G}} \cdot \underline{\boldsymbol{x}}$.

On the other pairs of faces F_2 and F_3, the heat flux is prescribed such that:

$$\underline{\boldsymbol{q}} \cdot \underline{\boldsymbol{n}} = 0 \quad \forall \underline{\boldsymbol{x}} \in \left(F_2 \cap \partial V_f^{\text{out}} \right) \cup \left(F_3 \cap \partial V_f^{\text{out}} \right) \qquad (41)$$

From Eq. (22), it follows:

$$\langle T_{,1} \rangle = G_1 \qquad (42)$$

with $T_{,1} = \frac{\partial T}{\partial x_1}$.

The macroscopic heat flux field is computed using Eq. (24). Details of the calculation can be found in Appendix B.

3.4. Boundary conditions for mechanical variables

3.4.1. Kinematic uniform boundary conditions – KUBC

The macroscopic strain tensor $\mathbf{E}$ is prescribed at the boundary ∂V of the simulation domain, such that:

$$\underline{u} = \underset{\sim}{\mathbf{E}} \cdot \underline{x} \quad \forall \underline{x} \in \partial V = \partial V_f^{out} \cup \partial V_p^{out} \tag{43}$$

which yields,

$$\langle \underset{\sim}{\boldsymbol{\varepsilon}} \rangle = \frac{1}{V} \int_{\partial V} (\underset{\sim}{\mathbf{E}} \cdot \underline{x}) \underline{n} \, dS = \underset{\sim}{\mathbf{E}} \tag{44}$$

The macroscopic stress field $\underset{\sim}{\Sigma}$ is computed in this way:

$$\underset{\sim}{\Sigma} = \langle \underset{\sim}{\boldsymbol{\sigma}} \rangle = V_V^f \langle \underset{\sim}{\boldsymbol{\sigma}} \rangle_f \tag{45}$$

3.4.2. Static uniform boundary conditions – SUBC

Let us now consider the case of a macroscopic traction vector prescribed at the boundary ∂V of the simulation domain, such that for a given uniform tensor $\underset{\sim}{\Sigma}$:

$$\underset{\sim}{\boldsymbol{\sigma}} \cdot \underline{n} = \underset{\sim}{\Sigma} \cdot \underline{n} \quad \forall \underline{x} \in \partial V \tag{46}$$

In the case of Poisson fibers, this condition is in conflict with the extension of the stress field:

$$\underset{\sim}{\boldsymbol{\sigma}} = 0 \quad \forall \underline{x} \in V_p \tag{47}$$

so that,

$$\underset{\sim}{\boldsymbol{\sigma}} \cdot \underline{n} = 0 \quad \forall \underline{x} \in \partial V_p \tag{48}$$

We can only prescribe:

$$\underset{\sim}{\boldsymbol{\sigma}} \cdot \underline{n} = \underset{\sim}{\Sigma} \cdot \underline{n} \quad \forall \underline{x} \in \partial V_f^{out} \tag{49}$$

but in the case of a random microstructure, these BC do not ensure static equilibrium:

$$\int_{\partial V} \underset{\sim}{\boldsymbol{\sigma}} \cdot \underline{n} \, dS = \underline{0} \tag{50}$$

since $\int_{\partial V_f^{out}} \underset{\sim}{\Sigma} \cdot \underline{n} \, dS$ does not necessarily vanish.

That is why the following alternative BC are proposed.

3.4.3. Mixed mechanical boundary conditions – MBC

A mixed type of BC is proposed here, instead of SUBC, in order to compute values that we can compare with those obtained using KUBC. Since only a minimal number of DOFs are prescribed on the boundary ∂V, mixed mechanical boundary conditions (MBC) are less constraining, or "softer", than KUBC. They differ from the mixed uniform boundary conditions (MUBC) proposed in Hazanov and Huet (1994) and Hazanov (1998) which are restricted, in general, to tensile loading of a volume element. They also differ from the normal mixed BC (NMBC) proposed by Gélébart et al. (2009), since those are applied on the whole boundary ∂V, similarly to MUBC. The periodicity compatible mixed uniform boundary conditions (PMUBC) were proposed by Pahr et al. (2008) as a generalization of MUBC, and implemented by Chateau et al. (2010). The BC proposed here are similar to PMUBC, but simpler because only 2 loading configurations are considered. MBC are considered with a view to estimating the overall bulk and shear moduli of isotropic random porous media, thus being less general than PMUBC; the 2 loading cases are presented hereafter.

Mixed triaxial loading. Displacement $\underline{u}$ is prescribed along normals on ∂V, such that:

$$u_1 = E_{11}x_1 \quad \forall \underline{x} \in F_1$$
$$u_2 = E_{22}x_2 \quad \forall \underline{x} \in F_2$$
$$u_3 = E_{33}x_3 \quad \forall \underline{x} \in F_3 \tag{51}$$

The traction vector $\underset{\sim}{\boldsymbol{\sigma}} \cdot \underline{n}$ is prescribed in this way:

$$\sigma_{21}n_1 = \sigma_{31}n_1 = 0 \quad \forall \underline{x} \in F_1$$
$$\sigma_{12}n_2 = \sigma_{32}n_2 = 0 \quad \forall \underline{x} \in F_2$$
$$\sigma_{13}n_3 = \sigma_{23}n_3 = 0 \quad \forall \underline{x} \in F_3 \tag{52}$$

From Eq. (27), it yields:

$$\langle \varepsilon_{11} \rangle = E_{11}; \quad \langle \varepsilon_{22} \rangle = E_{22}; \quad \langle \varepsilon_{33} \rangle = E_{33} \tag{53}$$

The macroscopic stress is computed using Eq. (29).

Mixed shear loading. Displacement $\underline{u}$ is prescribed along direction 1 on F_2 and direction 2 on F_1, such that:

$$u_2 = E_{12}x_1 \quad \forall \underline{x} \in F_1$$
$$u_1 = E_{12}x_2 \quad \forall \underline{x} \in F_2 \tag{54}$$

Two components of the traction vector $\underset{\sim}{\boldsymbol{\sigma}} \cdot \underline{n}$ are prescribed in this way:

$$\sigma_{11}n_1 = \sigma_{31}n_1 = 0 \quad \forall \underline{x} \in F_1$$
$$\sigma_{22}n_2 = \sigma_{32}n_2 = 0 \quad \forall \underline{x} \in F_2 \tag{55}$$

The traction vector is fully prescribed on F_3:

$$\sigma_{33}n_3 = \sigma_{13}n_3 = \sigma_{23}n_3 = 0 \quad \forall \underline{x} \in F_3 \tag{56}$$

Eq. (27) gives:

$$\langle \varepsilon_{12} \rangle = E_{12} \tag{57}$$

Details of the calculation can be found in Appendix C. Again, the macroscopic stress is computed using Eq. (29). The boundary value problems for estimating the overall bulk and shear moduli are explicited hereafter for both KUBC and MBC.

3.5. Overall properties

Heat transfer is assumed to take place within the fibers and be defined locally according to Fourier's law:

$$\underline{q} = -\lambda \nabla T \quad \forall \underline{x} \in V_f \tag{58}$$

with λ, thermal conductivity of the thermally isotropic fibers.

Regarding mechanical behavior, the fibers are considered linear elastic following the generalized Hooke law:

$$\underset{\sim}{\boldsymbol{\sigma}} = \underset{\approx}{\mathbf{c}} : \underset{\sim}{\boldsymbol{\varepsilon}} \quad \forall \underline{x} \in V_f \tag{59}$$

with $\mathbf{c}$, fourth-order positive definite tensor of elastic moduli of the isotropic elastic fibers.

3.5.1. Overall thermal conductivity

The homogeneous equivalent medium (overall material) considered in this work is isotropic; for the case of linear thermal heat conduction, $-\langle \underline{q} \cdot \nabla T \rangle$ is used as an estimate of $\lambda^{eff} \underline{G} \cdot \underline{G}$, where λ^{eff} is the effective thermal conductivity of the homogenized medium. The following macroscopic gradient of temperature is considered:

$$\underline{G} = \begin{bmatrix} -1 \\ 0 \\ 0 \end{bmatrix} \tag{60}$$

so that,

$$T_0 \mathcal{D}\text{th} = \langle -\underline{q} \cdot \nabla T \rangle = -\underline{Q} \cdot \underline{G} = \lambda^{eff} \underline{G} \cdot \underline{G} = \lambda^{eff} \tag{61}$$

When computed on a given volume element that is not necessarily representative, $\lambda^{app} = \langle -\underline{q} \cdot \nabla T \rangle$ is an estimate of λ^{eff}.

3.5.2. Overall bulk modulus

For the case of linear elasticity, $\langle \underset{\sim}{\boldsymbol{\sigma}} : \underset{\sim}{\boldsymbol{\varepsilon}} \rangle$ is used as an estimate of $\left(\underset{\approx}{\mathbf{C}}^{\text{eff}} : \underset{\sim}{\mathbf{E}} \right) : \underset{\sim}{\mathbf{E}}$, with $\underset{\approx}{\mathbf{C}}^{\text{eff}}$, the tensor of effective elastic moduli of the homogenized medium, that can be rewritten in this way:

$$\underset{\approx}{\mathbf{C}}^{\text{eff}} = 3k^{\text{eff}} \underset{\approx}{\mathbf{J}} + 2\mu^{\text{eff}} \underset{\approx}{\mathbf{K}} \tag{62}$$

with $\mathbf{K}$ and $\mathbf{J}$ respectively deviatoric and spherical projector on 2nd-order tensors.

Hence, for a hydrostatic macroscopic strain tensor,

$$\underset{\sim}{\mathbf{E}} = \begin{bmatrix} 1 & 0 & 0 \\ 0 & 1 & 0 \\ 0 & 0 & 1 \end{bmatrix} \tag{63}$$

it yields:

$$2\mathcal{E}^{\text{el}} = \langle \underset{\sim}{\boldsymbol{\sigma}} : \underset{\sim}{\boldsymbol{\varepsilon}} \rangle = \underset{\sim}{\boldsymbol{\Sigma}} : \underset{\sim}{\mathbf{E}} = \left(\underset{\approx}{\mathbf{C}}^{\text{eff}} : \underset{\sim}{\mathbf{E}} \right) : \underset{\sim}{\mathbf{E}} = 3k^{\text{eff}} \underset{\sim}{\mathbf{E}} : \underset{\approx}{\mathbf{J}} : \underset{\sim}{\mathbf{E}} = 9k^{\text{eff}} \tag{64}$$

When computed on a given volume element, $k^{\text{app}} = \frac{1}{9} \langle \underset{\sim}{\boldsymbol{\sigma}} : \underset{\sim}{\boldsymbol{\varepsilon}} \rangle$ is an estimate of k^{eff}.

3.5.3. Overall shear modulus

For a deviatoric macroscopic strain tensor,

$$\underset{\sim}{\mathbf{E}} = \begin{bmatrix} 0 & \frac{1}{2} & 0 \\ \frac{1}{2} & 0 & 0 \\ 0 & 0 & 0 \end{bmatrix} \tag{65}$$

it yields:

$$2\mathcal{E}^{\text{el}} = \langle \underset{\sim}{\boldsymbol{\sigma}} : \underset{\sim}{\boldsymbol{\varepsilon}} \rangle = \underset{\sim}{\boldsymbol{\Sigma}} : \underset{\sim}{\mathbf{E}} = \left(\underset{\approx}{\mathbf{C}}^{\text{eff}} : \underset{\sim}{\mathbf{E}} \right) : \underset{\sim}{\mathbf{E}} = 2\mu^{\text{eff}} \underset{\sim}{\mathbf{E}} : \underset{\approx}{\mathbf{K}} : \underset{\sim}{\mathbf{E}} = \mu^{\text{eff}} \tag{66}$$

When computed on a given volume element, $\mu^{\text{app}} = \langle \underset{\sim}{\boldsymbol{\sigma}} : \underset{\sim}{\boldsymbol{\varepsilon}} \rangle$ is an estimate of μ^{eff}.

4. Results

The estimation of thermal and elastic properties is now performed on hundreds of realizations. Fibers were attributed the constitutive material properties listed in Table 2. The variability of each realization gives rise to different results for morphological and apparent thermal and elastic properties. Mean values over n realizations of the same size are considered in this section. The number of realizations n fluctuates, depending on the size and BC. Ideally, n should be different for each volume size in order to achieve a similar measurement error for all sizes considered. The fluctuation observed here is due to errors during the meshing step; the larger the virtual sample, the more defects in the geometry are likely to happen. Nevertheless, the values gathered in Table 3 are large enough for achieving statistical representativity.

4.1. Morphological properties

The mean volume fraction of fibers $\overline{V_V^f}$ over n realizations for a given volume size V is computed using FE as follows:

$$\overline{V_V^f} = \frac{1}{n} \sum_{i=1}^{n} (V_V^f)_i = \frac{1}{n} \sum_{i=1}^{n} \left(\frac{1}{V} \int_V 1_{V_f} dV \right)_i \tag{67}$$

with 1_{V_f} being the indicator function of the fiber phase.

The numbers of realizations considered for estimating the volume fraction correspond to the first line in Table 3. These mean values $\overline{V_V^f}$ are then plotted as a function of the volume of simulation in Fig. 7. The mean value obtained for $V = 10^6$ is $\overline{V_V^f} = 16.2\% \pm 1.3\%$. Fluctuations are inherent to the morphological stochastic modeling. As expected, no bias of the volume fraction occurs, whatever the size of the realizations.

4.2. Thermal properties

Results for the thermal properties are obtained over a large number of realizations (between 19 and 64, depending on their size). The ensemble averaged apparent thermal conductivity $\overline{\lambda^{\text{app}}}$ is computed in this way:

$$\overline{\lambda^{\text{app}}} = \frac{1}{n} \sum_{i=1}^{n} (\lambda^{\text{app}})_i = \frac{1}{n} \sum_{i=1}^{n} \left(\langle -\underline{\mathbf{q}} \rangle_f \cdot \underline{\mathbf{G}} \right)_i \tag{68}$$

The discrepancy error $\Delta(\overline{Z})$ between minimal and maximal estimates computed for different boundary conditions, for a given volume size, is obtained as follows:

$$\Delta(\overline{Z}) = \frac{\overline{Z_{\max}} - \overline{Z_{\min}}}{\overline{Z_{\min}}} \tag{69}$$

Results for the mean apparent thermal conductivity $\overline{\lambda^{\text{app}}}$ are shown on Fig. 8 as a function of the volume and corresponding number of fibers considered. The mean values obtained for the largest system size considered ($\overline{N} \simeq 800$) are shown with the corresponding intervals of confidence $[\overline{Z} \pm 2D_Z]$ in Table 4 and compared to analytical bounds. Mean values obtained with UTG are slightly decreasing with increasing volume size, while mean values obtained with MTBC are increasing. The discrepancy error on the mean value between UTG and MTBC for the largest sample considered is $\Delta\left(\overline{\lambda^{\text{app}}}\right) = 16\%$. The mean value has converged towards an effective value for a volume $V = 50^3$ containing at least 180 fibers. Hence, the effective thermal conductivity is determined from the mean apparent values for the largest sample considered: $\lambda^{\text{eff}} = 6.57 \pm 1.45$ W.$[L]^{-1}$.K^{-1}. The standard deviation D_Z is also decreasing with increasing volume size, the analysis of this trend is postponed to Section 5.3.

4.3. Elastic properties

As for the thermal properties of fibers, results for the elastic properties are obtained over a large number of realizations (between 12 and 63, depending on their size). For the hydrostatic loading defined in Section 3.5.2, the ensemble averaged apparent bulk modulus $\overline{k^{\text{app}}}$ is computed in this way:

$$\overline{k^{\text{app}}} = \frac{1}{n} \sum_{i=1}^{n} (k^{\text{app}})_i = \frac{1}{n} \sum_{i=1}^{n} \left(\frac{1}{9} \langle \text{Tr} \, \underset{\sim}{\boldsymbol{\sigma}} \rangle_f \right)_i \tag{70}$$

On the other hand, the ensemble averaged apparent shear modulus $\overline{\mu^{\text{app}}}$ is obtained as follows for the shear loading defined in Section 3.5.3:

$$\overline{\mu^{\text{app}}} = \frac{1}{n} \sum_{i=1}^{n} (\mu^{\text{app}})_i = \frac{1}{n} \sum_{i=1}^{n} \left(\langle \sigma_{12} \rangle_f \right)_i \tag{71}$$

Results for the bulk modulus $\overline{k^{\text{app}}}$ and shear modulus $\overline{\mu^{\text{app}}}$ are shown respectively on Figs. 9 and 10 for the different volumes of

Table 2
Constitutive material parameters for Poisson fibers.

Young's modulus (GPa)	210
Poisson's ratio	0.3
Shear modulus (GPa)	81
Bulk modulus (GPa)	175
Thermal conductivity (W.$[L]^{-1}$.K^{-1})	100
Volume fraction	0.16

Table 3
Number of realizations n considered depending on boundary conditions and simulation size.

BC	Volume									
	10^3	20^3	30^3	40^3	50^3	60^3	70^3	80^3	90^3	100^3
$n - \text{UTG} - \overline{\lambda^{\text{app}}}$	64	64	62	60	56	56	53	58	39	21
$n - \text{MTBC} - \overline{\lambda^{\text{app}}}$	51	63	60	56	50	46	48	46	30	19
$n - \text{KUBC} - \overline{k^{\text{app}}}$	63	63	61	60	56	54	44	51	32	13
$n - \text{KUBC} - \overline{\mu^{\text{app}}}$	63	63	61	60	54	54	47	50	27	14
$n - \text{MBC} - \overline{k^{\text{app}}}$	40	60	53	55	45	48	37	46	28	13
$n - \text{MBC} - \overline{\mu^{\text{app}}}$	41	62	58	59	48	49	45	41	11	12
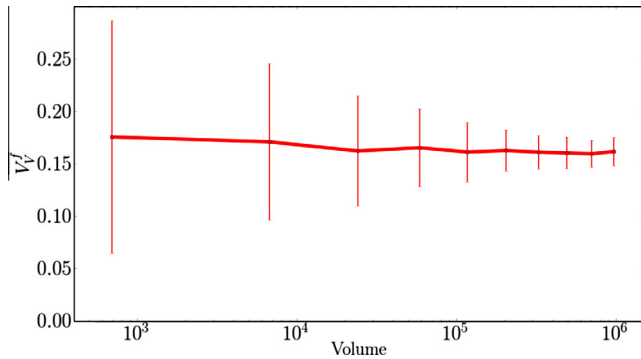
Fig. 7. Mean values for the volume fraction depending on the volume size V.
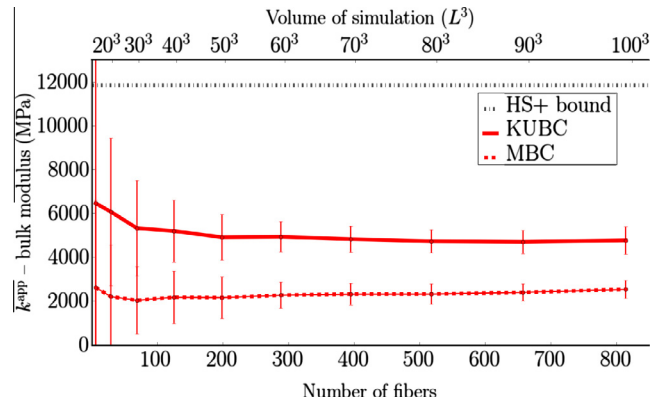
Fig. 9. Mean values for the bulk modulus depending on the number of fibers.
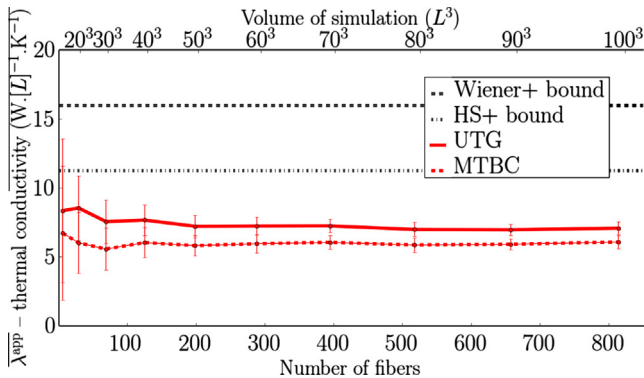
Fig. 8. Mean values for the thermal conductivity depending on the number of fibers.

Table 4
Bounds and mean values for apparent thermal and elastic properties.

	$\overline{k^{\text{app}}}$ (MPa)	$\overline{\mu^{\text{app}}}$ (MPa)	$\overline{\lambda^{\text{app}}}$ (W.[L]$^{-1}$.K^{-1})
FE-Uniform	4763 ± 624	3270 ± 394	7.07 ± 0.93
FE-Mixed	2527 ± 413	1097 ± 272	6.07 ± 0.97
Hashin–Shtrikman upper bound	11839	7328	11.27
Voigt bound/ Wiener upper bound	28000	12923	16.00

simulation and corresponding number of fibers ($\overline{N}$) considered. The mean values obtained for the largest system size considered ($\overline{N} \simeq 800$) are given with the corresponding intervals of confidence $[\overline{Z} \pm 2D_Z]$ in Table 4 and compared with analytical bounds. Boundary layer effects are significant for small elementary volume sizes, for both types of BC. Similarly to the results observed for the thermal properties, mean apparent values for Dirichlet-type BC (KUBC) are decreasing with increasing volume size, whereas mean estimates obtained with MBC are slightly increasing with V. There are very strong discrepancies for mean values obtained with KUBC and MBC for both bulk and shear moduli, even for the largest volume considered: $\Delta\left(\overline{k^{\text{app}}}\right) = 88\%$ and $\Delta\left(\overline{\mu^{\text{app}}}\right) = 198\%$. Apparent properties obtained for KUBC are constantly above those computed with MBC; this is in accordance with the bounds stated in Hazanov and Huet (1994) for mixed boundary conditions, as well as the hierarchies of estimates given by Huet (1997). Standard deviation is decreasing with increasing volume size, but its analysis is postponed to Section 5.3.

5. Discussion

The effective medium considered in this work is morphologically isotropic. Statistical isotropy of the thermal and elastic apparent properties will be discussed first, followed by an analysis of the local thermal and mechanical fields from the simulations. Finally the variance of properties is studied and consequences regarding the statistical representativity of simulations are drawn.

5.1. Statistical isotropy

5.1.1. Thermal conductivity

Firstly, the data computed for determining the mean apparent thermal conductivity $\overline{\lambda^{\text{app}}}$ is used to check for isotropy. This is done by checking that for the loading case defined in Section 3.5.1, the orthogonal components of the macroscopic heat flux vanish, i.e., $\overline{\langle q_2 \rangle} \to 0$ and $\overline{\langle q_3 \rangle} \to 0$ for an infinite medium, or an infinite number of realizations of a finite volume element. A non-dimensional discriminating criterion δ^λ is defined as follows:

$$\delta^\lambda = \frac{\left|\overline{\langle q_2 \rangle}\right| + \left|\overline{\langle q_3 \rangle}\right|}{|Q_1|} \tag{72}$$
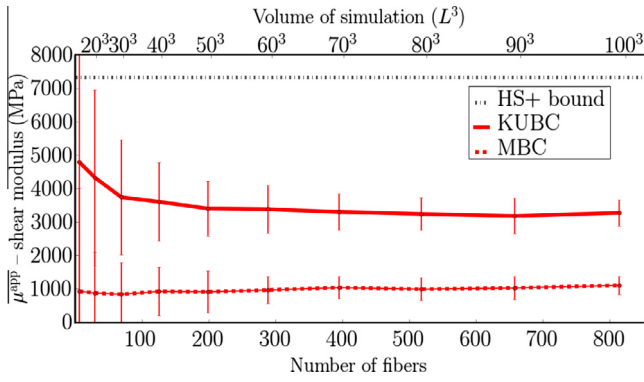
Fig. 10. Mean values for the shear modulus depending on the number of fibers.

The values for δ^λ are shown in Table 5 for the different volume sizes. Statistical isotropy of the thermal behavior can be assumed if $\delta^\lambda \ll 1$. δ^λ fluctuates between 10^{-3} and 2.7×10^{-2} for UTG and 2×10^{-3} and 8.4×10^{-2} for MTBC, yielding a very low degree of anisotropy.

5.1.2. Bulk modulus

The data computed for determining the mean apparent bulk modulus $\overline{k^{app}}$ is used. Considering the loading case defined in Section 3.5.2, isotropy is reached if $\sqrt{\langle \underset{\sim}{\sigma}^{dev} \rangle : \langle \underset{\sim}{\sigma}^{dev} \rangle} \to 0$, with $\underset{\sim}{\sigma}^{dev}$ the deviatoric stress tensor, for an infinite medium, or an infinite number of realizations of a finite volume element. A non-dimensional discriminating criterion δ^k is defined as follows:

$$\delta^k = \sqrt{\frac{\overline{\langle \underset{\sim}{\sigma} \rangle : \underset{\approx}{\mathbf{K}} : \langle \underset{\sim}{\sigma} \rangle}}{\overline{\langle \underset{\sim}{\sigma} \rangle : \underset{\approx}{\mathbf{J}} : \langle \underset{\sim}{\sigma} \rangle}}} = \sqrt{\frac{\overline{\langle \underset{\sim}{\sigma}^{dev} \rangle : \langle \underset{\sim}{\sigma}^{dev} \rangle}}{\overline{\langle \mathrm{Tr}\, \underset{\sim}{\sigma} \rangle^2}}} \tag{73}$$

The values for δ^k are shown in Table 6 for the considered volume sizes. Statistical isotropy can be assumed if $\delta^k \ll 1$. δ^k fluctuates between $< 10^{-3}$ and 3.1×10^{-2} for KUBC and 2×10^{-3} and 1.6×10^{-2} for MBC, thus yielding, like for thermal conductivity, a low degree of anisotropy.

5.1.3. Shear modulus

We will now use the data computed for determining the mean apparent shear modulus $\overline{\mu^{app}}$. Considering the loading case defined in Section 3.5.3, isotropy is reached if $\sqrt{\overline{\langle \mathrm{Tr}\, \underset{\sim}{\sigma} \rangle^2}} \to 0$ for an infinite medium, or an infinite number of realizations of a finite volume element. A non-dimensional discriminating criterion δ^μ is defined as follows:

$$\delta^\mu = \sqrt{\frac{\overline{\langle \underset{\sim}{\sigma} \rangle : \underset{\approx}{\mathbf{J}} : \langle \underset{\sim}{\sigma} \rangle}}{\overline{\langle \underset{\sim}{\sigma} \rangle : \underset{\approx}{\mathbf{K}} : \langle \underset{\sim}{\sigma} \rangle}}} = \sqrt{\frac{\overline{\langle \mathrm{Tr}\, \underset{\sim}{\sigma} \rangle^2}}{\overline{\langle \underset{\sim}{\sigma}^{dev} \rangle : \langle \underset{\sim}{\sigma}^{dev} \rangle}}} \tag{74}$$

The values for δ^μ are gathered on Table 7 as a function of the considered volume of the samples. Statistical isotropy can assumed if $\delta^\mu \ll 1$. It appears that δ^μ is fluctuating between $< 10^{-3}$ and 2.9×10^{-2} for KUBC, and 2×10^{-3} and 2×10^{-1} for MBC. These results show that for MBC, there is a higher degree of anisotropy

when considering the shear modulus than for the bulk modulus. Interestingly, this statement is reversed for KUBC. Discrepancies are observed on the elastic response for very small volumes with inherent fluctuations due to boundary layer effects, and very large volumes for which not enough realizations are available. They seem to be more pronounced for MBC, likely due to a slightly smaller number of realizations.

5.1.4. Tensor of apparent elastic moduli

Finally, using KUBC, the full elastic moduli tensor $\mathbf{C}_E^{app}$ was determined for 50 realizations of Poisson fibers with a simulation volume $V = 50^3$ which corresponds to $\overline{N} \simeq 180$ fibers for each sample. Details regarding the boundary value problems for determining the components of the elastic moduli tensor are given in Appendix A. The apparent elastic moduli tensor averaged over $n = 50$ realizations is presented in Eq. (75) with the corresponding intervals of confidence $[\overline{C_{IJ}} \pm 2D_{C_{IJ}}]$. The averaged tensor components obtained for $n = 50$ are characteristic of isotropic elasticity since $\overline{C_{11}} \approx \overline{C_{22}} \approx \overline{C_{33}}$ with a maximal error of 12%, $\overline{C_{12}} \approx \overline{C_{13}} \approx \overline{C_{23}}$ with $\epsilon_{rel} = 20\%$, $\overline{C_{44}} \approx \overline{C_{55}} \approx \overline{C_{66}}$ with $\epsilon_{rel} = 17\%$ and are approximately equal to $\frac{\overline{C_{11}} - \overline{C_{12}}}{2}$ with a relative error of 14% in the worst case. The remaining components vanish in the isotropic case; here, they represent not more than 1% of $\overline{C_{11}}$.

$$\overline{\overline{\underset{\approx}{\mathbf{C}}}}_{50} = \begin{bmatrix} 9627 \pm 2820 & 3002 \pm 740 & 3028 \pm 709 & 14 \pm 342 & -64 \pm 714 & 85 \pm 890 \\ \bullet & 8715 \pm 2401 & 2530 \pm 639 & 14 \pm 664 & 24 \pm 307 & 44 \pm 934 \\ \bullet & \bullet & 8630 \pm 2445 & 48 \pm 697 & -24 \pm 841 & 15 \pm 298 \\ \bullet & \bullet & \bullet & 2910 \pm 763 & 13 \pm 310 & 21 \pm 314 \\ \bullet & \bullet & \bullet & \bullet & 3408 \pm 836 & 13 \pm 344 \\ \bullet & \bullet & \bullet & \bullet & \bullet & 3389 \pm 872 \end{bmatrix} \text{MPa} \tag{75}$$

5.2. Thermal and mechanical fields

In order to explain the discrepancies observed on the mean apparent properties, let us analyze the thermal and mechanical fields coming out of the simulation done on a realization with $V = 50^3$. In the case of thermal conduction, the normalized heat flux $\frac{q_1}{Q_1}$, mainly percolating in-between F_1^+ and F_1^-, is very similar for UTG and MTBC as shown in Fig. 11, presented using a split-view for the normalized heat flux showed for two computations on the same sample using UTG (top) and MTBC (bottom). This representation allows to distinguish the local discrepancies on the resulting field concentration between the two sets of boundary conditions. Differences come from the thermal conduction taking place in the fibers intersecting F_2 and F_3 when considering UTG. This has a limited impact on the homogenized value λ^{app}. In contrast, in the case of elasticity, discrepancies in the macroscopic results can be explained from the local mechanical fields. For the triaxial loading, mapping of the normalized elastic energy density $\frac{\underset{\sim}{\sigma}:\underset{\sim}{\varepsilon}}{V_f \langle \underset{\sim}{\sigma}:\underset{\sim}{\varepsilon} \rangle_f}$ is presented on Fig. 12 for KUBC and MBC. From this figure, it can be seen that KUBC induce a higher elastic energy density level than with MBC. Also, the strain localization is affecting every fiber for KUBC, while only the favorably oriented fibers are deforming with MBC, resulting in a more homogeneous elastic strain energy density field with KUBC than with MBC. On

Table 5
Statistical isotropy of the apparent thermal conductivity for Poisson fibers.

BC	Volume									
	10^3	20^3	30^3	40^3	50^3	60^3	70^3	80^3	90^3	100^3
UTG – δ^λ	0.027	0.021	0.004	0.007	0.001	0.011	0.003	0.004	0.003	0.003
MTBC – δ^λ	0.084	0.008	0.008	0.007	0.002	0.001	0.003	0.004	0.003	0.002

Table 6
Statistical isotropy of the apparent bulk modulus for Poisson fibers.

BC	Volume									
	10^3	20^3	30^3	40^3	50^3	60^3	70^3	80^3	90^3	100^3
KUBC – δ^k	0.031	0.018	0.011	0.003	0.004	0.017	0.002	<0.001	0.006	0.005
MBC – δ^k	0.014	0.016	0.011	0.002	0.012	0.008	0.002	0.008	0.003	0.007

Table 7
Statistical isotropy of the apparent shear modulus for Poisson fibers.

BC	Volume									
	10^3	20^3	30^3	40^3	50^3	60^3	70^3	80^3	90^3	100^3
KUBC – δ^μ	0.010	0.029	0.002	<0.001	0.015	0.024	0.008	0.004	0.014	0.005
MBC – δ^μ	0.199	0.045	0.031	0.022	0.016	0.006	0.015	0.002	0.015	0.009
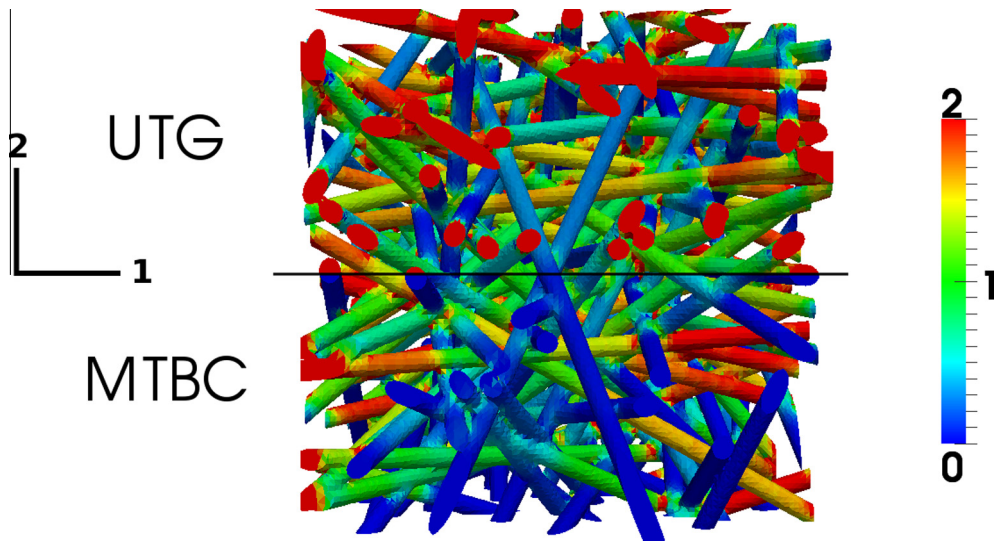
Fig. 11. $\frac{q_1}{Q_1}$ mapping for a $V = 50^3$ realization using UTG (top) and MTBC (bottom).
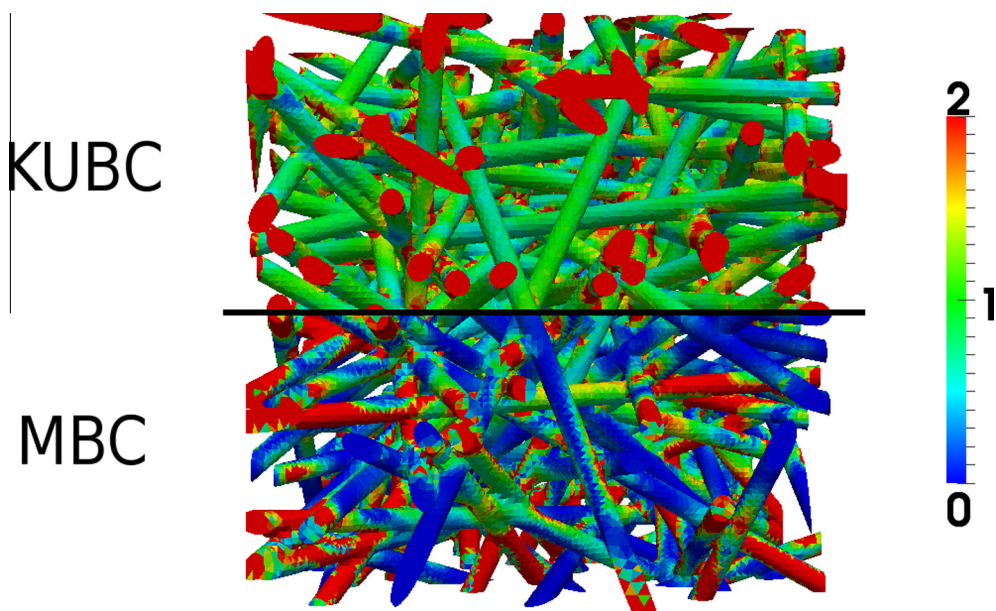
Fig. 12. $\frac{\sigma:\varepsilon}{V_f\langle\sigma:\varepsilon\rangle_f}$ mapping for a $V = 50^3$ realization under hydrostatic load using KUBC (top) and MBC (bottom).
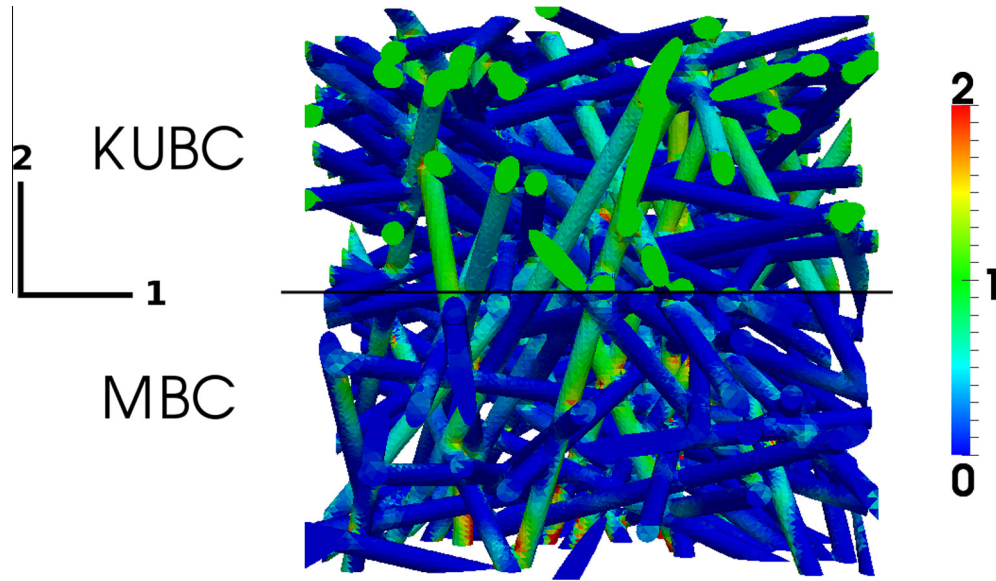
Fig. 13. $\frac{\varepsilon_{22}}{E_{22}}$ mapping for a $V = 50^3$ realization under hydrostatic load using KUBC (top) and MBC (bottom).
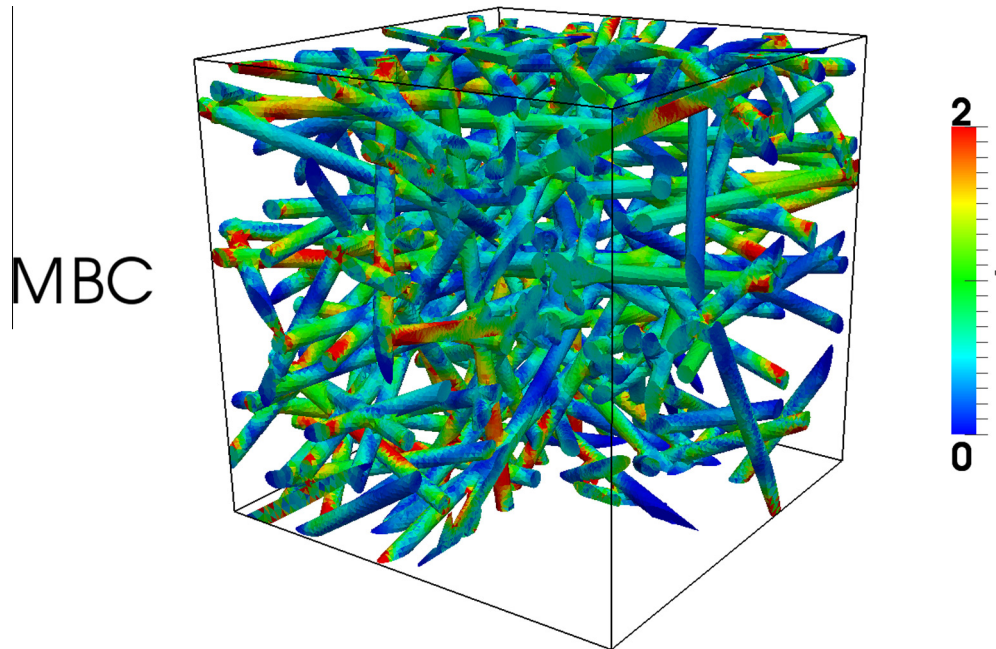

Fig. 14. $\frac{\sigma^{VM}}{\langle \sigma^{VM} \rangle}$ mapping for a $V = 50^3$ realization under hydrostatic load using MBC.

Fig. 13, mapping only $\frac{\varepsilon_{22}}{E_{22}}$, for MBC the localization is clearly confined to both ends of preferentially oriented fibers, here along the vertical direction. On the other hand, for KUBC most of the deformation takes place all over the boundary ∂V, including fibers that are not preferentially oriented. Bending of the fibers can be observed through the local stress field, as depicted on Fig. 14 which was clipped to show the normalized von Mises equivalent stress $\frac{\sigma^{VM}}{\langle \sigma^{VM} \rangle}$ within the fibers, here for the triaxial loading using MBC; $\sigma^{VM} = \sqrt{\frac{3}{2} \underset{\sim}{\boldsymbol{\sigma}}^{dev} : \underset{\sim}{\boldsymbol{\sigma}}^{dev}}$.

Table 8
Relative error for the samples considered ϵ_{rel} depending on boundary conditions and simulation size.

BC	Volume									
	10^3 (%)	20^3 (%)	30^3 (%)	40^3 (%)	50^3 (%)	60^3 (%)	70^3 (%)	80^3 (%)	90^3 (%)	100^3 (%)
$\epsilon_{rel} - \text{UTG} - \overline{\lambda^{app}}$	12.2	5.6	4.2	3.1	2.7	2.3	2.0	1.7	1.9	2.3
$\epsilon_{rel} - \text{MTBC} - \overline{\lambda^{app}}$	17.0	8.0	5.8	4.1	3.6	3.0	2.5	2.3	2.5	2.8
$\epsilon_{rel} - \text{KUBC} - \overline{k^{app}}$	9.9	4.9	3.7	2.9	2.5	2.1	2.0	1.7	1.9	2.6
$\epsilon_{rel} - \text{KUBC} - \overline{\mu^{app}}$	11.9	6.2	4.7	3.7	3.3	2.7	2.6	2.2	2.7	3.3
$\epsilon_{rel} - \text{MBC} - \overline{k^{app}}$	25.6	11.7	8.8	6.0	5.3	4.1	3.9	3.0	3.3	4.2
$\epsilon_{rel} - \text{MBC} - \overline{\mu^{app}}$	51.6	21.8	14.7	9.8	8.8	6.8	5.6	5.4	8.9	7.1

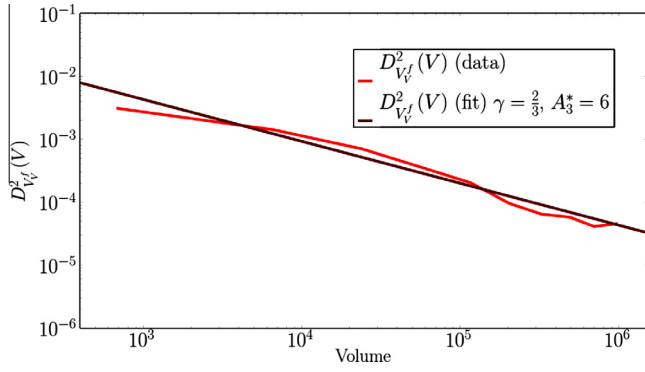**Fig. 15.** Variance for the volume fraction of fibers depending on the volume of simulation V.
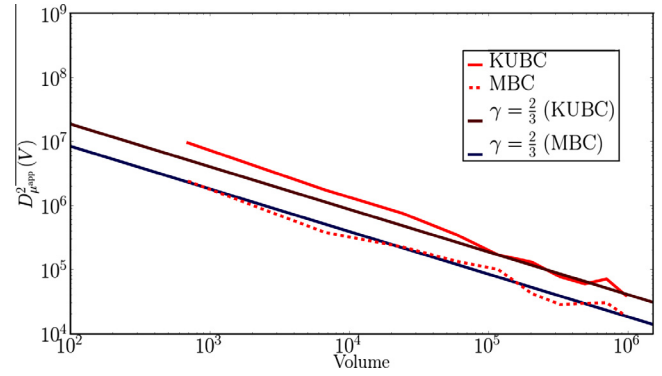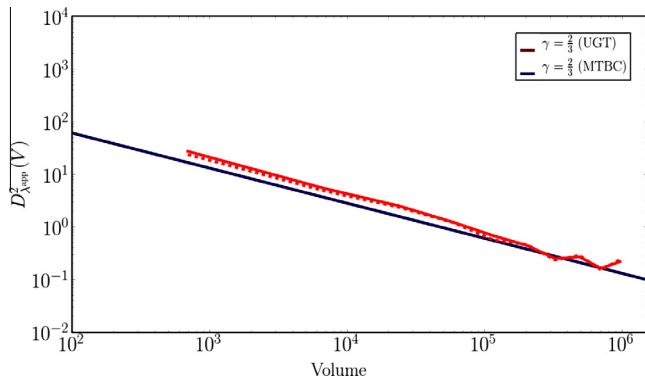

Fig. 16. Variance for the thermal conductivity depending on the volume of simulation V.
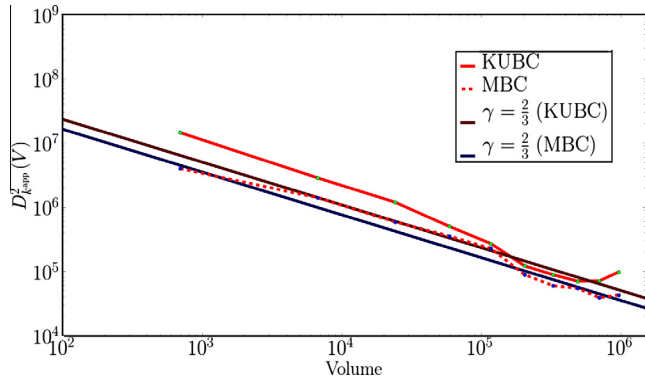

Fig. 17. Variance for the bulk modulus depending on the volume of simulation V.

5.3. Integral range, variance and RVE size

The physical interpretation of the integral range is such that for a given volume V, one can define $n = \frac{V}{A_3}$ volume elements for which the i averaged values $Z_i(V')$ over the n sub-volumes $V' = \frac{V}{n}$ are uncorrelated random variables. For a large specimen, i.e., $V \gg A_3$, the ensemble variance $D_Z^2(V)$ can then be expressed introducing the point variance of Z, D_Z^2 as follows (Matheron, 1971, 1989):

$$D_Z^2(V) = D_Z^2 \frac{A_3}{V} \tag{76}$$

with A_3, the integral range defined as:

$$A_3 = \frac{1}{D_Z^2} \int_{\mathbb{R}^3} \overline{W}_2(h)dh \tag{77}$$

Fig. 18. Variance for the shear modulus depending on the volume of simulation V.

Table 9
Values for γ exponent estimated from the simulation.

	γ
$\overline{\lambda^{\mathrm{app}}}$-UTG	0.68
$\overline{\lambda^{\mathrm{app}}}$-MTBC	0.64
$\overline{k^{\mathrm{app}}}$-KUBC	0.51
$\overline{k^{\mathrm{app}}}$-MBC	0.77
$\overline{\mu^{\mathrm{app}}}$-KUBC	0.64
$\overline{\mu^{\mathrm{app}}}$-MBC	0.66
$\overline{V_V^f}$	0.67

Table 10
RVE sizes estimated from computations with $\gamma = \frac{2}{3}, \epsilon_{\mathrm{rel}} = 5\%$ and $n = 1$.

Z	BC	K	V_{RVE}	$\overline{N}$
V_V	-	4.4×10^{-1}	164^3	2.1×10^3
λ^{app}	UTG	1.3×10^3	204^3	3.3×10^3
λ^{app}	MTBC	1.3×10^3	238^3	4.5×10^3
k^{app}	KUBC	5.0×10^8	188^3	2.8×10^3
k^{app}	MBC	3.5×10^8	296^3	6.9×10^3
μ^{app}	KUBC	4.0×10^8	245^3	4.8×10^3
μ^{app}	MBC	1.8×10^8	489^3	1.9×10^4

$\overline{W}_2(h)$ is the centered 2nd-order correlation function such that, for properties Z_f and Z_p respectively within the fibrous and porous phase, and probability p for $x \in V_f$:

$$\overline{W}_2(h) = \overline{(Z(x+h) - \overline{Z})(Z(x) - \overline{Z})} = (Z_f - Z_p)^2 (C(h) - p^2) \tag{78}$$

Following the method proposed by Matheron (1989) and implemented in Kanit et al. (2003), considering a large number n of realizations (or sub-volumes), the following absolute sampling error in the estimation of the effective properties arises:

$$\epsilon_{\mathrm{abs}} = \frac{2D_Z(V)}{\sqrt{n}} \tag{79}$$

From which the relative error ϵ_{rel} can be defined:

$$\epsilon_{\mathrm{rel}} = \frac{\epsilon_{\mathrm{abs}}}{\overline{Z}} = \frac{2D_Z(V)}{\overline{Z}\sqrt{n}} \Rightarrow \epsilon_{\mathrm{rel}}^2 = \frac{4D_Z^2 A_3}{\overline{Z}^2 nV} \tag{80}$$

Hence the following volume size can be considered as statistically representative for a prescribed property Z, number of realizations n and relative error (e.g., 5%):

$$V_{RVE} = \frac{4D_Z^2 A_3}{\epsilon_{rel}^2 \overline{Z}^2 n} \qquad (81)$$

This RVE size then depends on the point variance D_Z^2, integral range A_3 and mean value $\overline{Z}$. These three parameters are estimated from the simulations, except when considering the volume fraction, for which D_Z^2 is known explicitly:

$$D_{V_V^f}^2 = V_V^f(1 - V_V^f) \qquad (82)$$

The method presented just above has to be adapted to the case of Poisson fibers. Since the integral range of linear Poisson varieties is not finite (Jeulin, 1991), Eq. (76) does not apply anymore. It was proposed by Lantuéjoul (1991) to use a modified scaling law with exponent $\gamma < 1$. The variance can thus be rewritten as follows (Jeulin, 2011):

$$D_Z^2(V) = D_Z^2 \left(\frac{A_3^*}{V}\right)^\gamma \qquad (83)$$

A_3^* is not the integral of the centered second-order correlation function $\overline{W}_2(h)$ anymore. Nonetheless, it is homogeneous to a volume of material and can readily be used to determine RVE sizes which can then be obtained by updating the previous definition for relative error:

$$\epsilon_{rel} = \frac{\epsilon_{abs}}{\overline{Z}} = \frac{2D_Z(V)}{\overline{Z}\sqrt{n}} \Rightarrow \epsilon_{rel}^2 = \frac{4D_Z^2 A_3^{*\gamma}}{\overline{Z}^2 n V^\gamma} \qquad (84)$$

Hence yielding an updated definition of the RVE size:

$$V_{RVE} = A_3^* \left(\frac{4D_Z^2}{\epsilon_{rel}^2 \overline{Z}^2 n}\right)^{\frac{1}{\gamma}} \qquad (85)$$

Using Eq. (84), the relative error associated with the number of realizations considered (cf. Table 3) is computed and presented in Table 8. As stated in Section 4, ideally, the error should be the same for all sample series by adapting the number of realizations. Although the relative error fluctuates, most values are very low, except for the smallest sample sizes.

The generalized integral range A_3^* and scaling-law exponent γ can be estimated from simulations as it was done in Kanit et al. (2003) and Altendorf (2011). When considering statistical RVE sizes of microstructures with non-finite integral range for other properties than morphological ones, for which there is no information about the theoretical value of the point variance D_Z^2, it may be useful to reformulate Eq. (83) as follows:

$$D_Z^2(V) = KV^{-\gamma} \qquad (86)$$

with $K = D_Z^2 A_3^{*\gamma}$, leaving only 2 parameters to identify from the statistical data obtained by simulation. We use this last formulation for studying the thermal and elastic properties. Eq. (85) now reads as follows:

$$V_{RVE} = \left(\frac{4K}{\epsilon_{rel}^2 \overline{Z}^2 n}\right)^{\frac{1}{\gamma}} \qquad (87)$$

Results regarding the volume fraction are presented on Fig. 15. Variance for the apparent thermal conductivity, bulk and shear moduli as functions of the volume are shown on Figs. 16–18.

The γ exponents of the scaling-law for each physical property were estimated from the results of simulations, by fitting the slope of the variance curves. For the apparent thermal and elastic properties, only the data points for volumes $V \geq 40^3$ have been considered, in order to mitigate any bias due to boundary layer effects with small volumes. The values obtained in this way are gathered in Table 9. For the case of Poisson fibers, Jeulin (2011) gave the theoretical value of $\frac{2}{3}$ for γ in Eq. (83) and (86). This value holds only for the indicator function of the Poisson fibers and its mean value, the volume fraction. The value estimated here ($\gamma = 0.67$) verifies the theoretical result of Jeulin (2011). Results from Altendorf (2011), for 3D randomly distributed long-fibers, show a convergence of the variance on the volume fraction of fibers following a scaling law with exponent $\gamma = 0.87$; this value is in-between the values for infinite fibers ($\gamma = \frac{2}{3}$) and short-fibers ($\gamma = 1$), which could be compared to a random distribution of spheres in the extreme case of a shape factor equal to 1, similarly to the simulations in Jean et al. (2011). For both apparent thermal conductivity and shear modulus, γ fluctuates between 0.64 and 0.68. Hence, as a 1st-order approximation, these physical properties may depend on the indicator function of the fibers. The same conclusion can be drawn for the apparent bulk modulus, but with further variation since γ varies between 0.51 and 0.77 depending on the BC. These fluctuations are most likely due to inaccuracies in fitting and approximations in the virtual samples geometry.

For the sake of comparing the representativity of samples for different properties, and since the values estimated from the simulations are close to the theoretical value $\gamma = \frac{2}{3}$, this value will be used for all the results from now on. From Eq. (86), γ being prescribed, K is the only parameter left for fitting the data.

Using Eq. (85), it is now possible to determine statistical RVE sizes from computational simulations. K is estimated numerically from Eq. (86) and estimates for RVE sizes are presented in Table 10 for a relative error of 5% in the case a single realization ($n = 1$). RVE sizes presented in this table are always larger than the volume element sizes achieved throughout this work: $V = 100^3$ for the largest. This concurs with the discrepancies observed on the apparent elastic moduli; as a matter of fact, the response over an elementary volume should be independent of the BC once RVE size is reached as stated by Sab (1992), but the proof given in this reference does not hold in the case of an elementary volume including a porous phase intersecting the boundary ∂V; this remains an open question. Even if the MBC used in this work differ from the MUBC proposed by Hazanov and Huet (1994), one could consider the MBC estimates to be closer to the effective values than the KUBC estimates; this was shown for MBC theoretically in Hazanov and Huet (1994), Huet (1997) and experimentally in Hazanov and Amieur (1995).

Nevertheless, the precision for a given volume can be obtained from multiple realizations of smaller volumes. As an example, for k^{app} with KUBC, if $V = 50^3$, and $\epsilon_{rel} = 5\%$, one must compute 18 realizations to attain the same statistical convergence as for 1 realization of $V = 188^3$. Precaution should be taken regarding the bias induced by boundary layer effects on mean values when choosing smaller elementary volumes: virtual samples that are too small should be excluded.

Finally, values for RVE size and relative error in Table 10 can be compared to the volume considered and associated relative error in Table 8: for instance, if one considers the experimental error associated with the estimate of $\overline{k^{app}}$ using KUBC for $V = 100^3$, with $n = 13$ realizations, $\epsilon_{rel} = 2.6\%$. For the same relative error and number of realizations, the asymptotic model, on which values in Table 10 are based, yields an RVE size of $V = 100.1^3$, which corresponds to an error of 0.1%. The model is thus appropriate for every data point considered, except in the case of volumes for which boundary layer effects are not negligible.

6. Conclusions

Poisson fibers are undoubtedly one of the worst case scenario one could think of in terms of homogenizing random media: this microstructure cannot be periodized, presents an infinite contrast of properties, includes an interconnected porous phase that is intersecting the outer boundary of the samples considered, and has an infinite integral range. These features make this type of random media interesting for testing the robustness of the statistical approach that was introduced in Kanit et al. (2003) for determining RVE sizes. This study questions the applicability of the concept of RVE for pathological cases such as Poisson fibers. The microstructural model was developed and implemented numerically. Hundreds of realizations were computed using FE, generating a large amount of data to be analyzed statistically. The main results arising from the study of Poisson fibers can be summarized as follows:

- Neumann-type boundary conditions (SUBC and UHF) are incompatible with the considered microstructure. Two alternative sets of boundary conditions were proposed.
- Thermal and elastic effective properties were estimated by the apparent values obtained for uniform and mixed boundary conditions. Convergence of mean values was reached for thermal properties; the effective thermal conductivity was subsequently determined.
- Discrepancies on mean values were observed for mean apparent elastic properties between KUBC and MBC. This could be symptomatic of either non-homogenizability, i.e., BC-dependent response of the medium, or gigantic RVE sizes. Because of the results for thermal conductivity, the latter seems more likely.
- Values for apparent properties obtained with Dirichlet-type boundary conditions (KUBC and UTG) are larger than those computed with mixed boundary conditions, this is in accordance with theoretical results given by Huet (1997).
- The study of the ensemble variance for apparent properties gave rise to scaling power-laws of exponent γ. This exponent was obtained from computational experiments, and folllowed approximately the theoretical value $\gamma = \frac{2}{3}$ given by Jeulin (2011). This entails that the thermal dissipation rate and elastic energy densities depend on the indicator function of the fibers as a 1st-order approximation.
- Very large RVE sizes were determined for a given relative error with a single realization only. A similar precision can be obtained with full-field approaches on smaller samples if multiple realizations are considered.

Further work should include more simulations in order to get better statistics; larger samples should also be investigated, especially for the mechanical case. To do so, domain-decomposition approaches for parallel computing, which could not be applied in the present work, should be considered. From a materials science viewpoint, samples could be manufactured using 3D printing and mechanically characterized, as done in Dirrenberger et al. (2013). In non-woven random fibrous materials, bonding and friction between fibers are significant in terms of mechanical behavior, thus Poisson fibers generated using a hard-core repulsion model should be considered instead of a continuous medium of interpenetrating fibers.

Overall, the method proposed in Kanit et al. (2003) for determining RVE sizes was found to be operational, even for pathological microstructures. A prerequisite for the use of this statistical approach is that convergence of effective properties is achieved. However, the application of the method in spite of the absence of convergence provides an estimation of the RVE size which might be strongly biased. The merit of the approach is at least to provide an estimate which can then guide future effort based on more powerful computing methods able to process larger volume sizes.

In order to go one step further, one could apply the same statistical approach to Poisson planes, which are another Poisson linear variety, but with a scaling power-law of exponent $\gamma = \frac{1}{3}$ (Jeulin, 2011), leading to even stronger constraints for the convergence of volume averaged properties, as required in the estimation of effective properties.

Appendix A. Determination of elastic moduli components using KUBC

Using the generalized Hooke law, 6 different computations have to be performed to determine the full elastic moduli tensor. For instance, in order to compute the components C_{2I}^{app}, the following macroscopic strain tensor $\underset{\sim}{\mathbf{E}}$ is considered:

$$\underset{\sim}{\mathbf{E}} = \begin{bmatrix} 0 & 0 & 0 \\ 0 & 1 & 0 \\ 0 & 0 & 0 \end{bmatrix} \tag{A.1}$$

Using Hooke's law, the apparent elastic moduli $\underset{\approx}{\mathbf{C}}^{\text{app}}$ are defined:

$$\underset{\sim}{\mathbf{\Sigma}} = \underset{\approx}{\mathbf{C}}^{\text{app}} : \underset{\sim}{\mathbf{E}} \tag{A.2}$$

The following linear relationships arise for C_{2I}^{app}:

$$\Sigma_{11} = C_{12}^{\text{app}} E_{22}$$
$$\Sigma_{22} = C_{22}^{\text{app}} E_{22}$$
$$\Sigma_{33} = C_{23}^{\text{app}} E_{22}$$
$$\Sigma_{23} = C_{24}^{\text{app}} E_{22}$$
$$\Sigma_{31} = C_{25}^{\text{app}} E_{22}$$
$$\Sigma_{12} = C_{26}^{\text{app}} E_{22} \tag{A.3}$$

The other components of C_{IJ}^{app} are computed in a similar way.

Appendix B. Detailed calculation for mixed thermal boundary conditions

Let us consider the spatial average of the temperature gradient:

$$\langle \nabla T \rangle = \frac{1}{V} \int_V \nabla T \, dV = \frac{1}{V} \int_{\partial V} T \underline{\boldsymbol{n}} \, dS$$
$$= \frac{1}{V} \int_{F_1} T \underline{\boldsymbol{n}} \, dS + \frac{1}{V} \int_{F_2 \cup F_3} T \underline{\boldsymbol{n}} \, dS \tag{B.1}$$

For a coordinates system with its origin at the center of the simulation cube, each component of the temperature gradient is considered. It yields:

$$\langle T_{,1} \rangle = \frac{1}{V} \int_{F_1} T n_1 \, dS = \frac{1}{V} \int_{F_1^+} T n_1 \, dS - \frac{1}{V} \int_{F_1^-} T n_1 \, dS = \frac{1}{V} \int_{F_1} \underline{\boldsymbol{G}} \cdot \underline{\boldsymbol{x}} n_1 \, dS$$

$$= \frac{1}{V} \underline{\boldsymbol{G}} \int_{F_1} \underline{\boldsymbol{x}} n_1 \, dS = \frac{1}{V} \left(G_1 \int_{F_1} x_1 n_1 \, dS + G_2 \underbrace{\int_{F_1} x_2 n_1 \, dS}_{=0} + G_3 \underbrace{\int_{F_1} x_3 n_1 \, dS}_{=0} \right) = G_1 \tag{B.2}$$

Now for the other components, for instance:

$$\langle T_{,2} \rangle = \frac{1}{V} \int_{F_2} T n_2 \, dS = \frac{1}{V} \int_{F_2^+} T n_2 \, dS - \frac{1}{V} \int_{F_2^-} T n_2 \, dS = \frac{1}{V} \int_{F_2^+ \cap \partial V_f^{out}} T n_2 \, dS$$

$$+ \int_{F_2^+ \cap \partial V_p^{out}} T n_2 \, dS - \int_{F_2^- \cap \partial V_f^{out}} T n_2 \, dS - \int_{F_2^- \cap \partial V_p^{out}} T n_2 \, dS \qquad (B.3)$$

In our computations the surface integral over $\partial V_f^{out} \cap F_2$ can be evaluated. However, a suitable extrapolation of T on $\partial V_p^{out} \cap F_2$ is needed for the full evaluation of $\langle T_{,2} \rangle$. The same argument holds for $\langle T_{,3} \rangle$.

Let us now consider the macroscopic heat flux, using Eq. (23):

$$\underline{Q} = V_V^f \langle \underline{q} \rangle_f = \frac{1}{V} \int_{\partial V_f^{out}} \left(\underline{q} \cdot \underline{n} \right) \underline{x} \, dS \qquad (B.4)$$

So, for each component:

$$Q_i = \frac{1}{V} \int_{\partial V_f^{out}} \left(\underline{q} \cdot \underline{n} \right) x_i \, dS = \frac{1}{V} \int_{F_1 \cap \partial V_f^{out}} \left(\underline{q} \cdot \underline{n} \right) x_i \, dS$$

$$= \frac{1}{V} \int_{F_1^+} q_1 x_i \, dS - \frac{1}{V} \int_{F_1^-} q_1 x_i \, dS \qquad (B.5)$$

which yields,

$$Q_1 = \frac{1}{V} L \int_{F_1^+} q_1 \, dS \qquad (B.6)$$

In our computation, Q_1 is actually post-processed by means of the following spatial average:

$$Q_1 = V_V^f \langle q_1 \rangle_f \qquad (B.7)$$

Components Q_2 and Q_3 are estimated in the same fashion. They do not vanish in general.

Appendix C. Detailed calculation for mixed mechanical boundary conditions

C.1. Triaxial loading

Let us consider the spatial average of the strain:

$$\langle \underset{\sim}{\varepsilon} \rangle = \frac{1}{V} \int_V \underset{\sim}{\varepsilon} \, dV = \frac{1}{V} \int_{\partial V} \underline{u} \overset{s}{\otimes} \underline{n} \, dS = \frac{1}{V} \int_{\partial V} u_i n_j \, dS \, \underline{e}_i \otimes \underline{e}_j \qquad (C.1)$$

If we now consider each component of the strain field for the case of a coordinates system with its origin at the center of the cube, it yields:

$$\langle \varepsilon_{11} \rangle = \frac{1}{V} \int_V \varepsilon_{11} \, dV = \frac{1}{V} \int_V u_{1,1} \, dV = \frac{1}{V} \int_{\partial V} u_1 n_1 \, dS$$

$$= \frac{1}{V} \left(\int_{F_1} u_1 n_1 \, dS + \underbrace{\int_{F_2} u_1 n_1 \, dS}_{=0} + \underbrace{\int_{F_3} u_1 n_1 \, dS}_{=0} \right) = \frac{1}{V} \int_{F_1} E_{11} x_1 n_1 \, dS$$

$$= \frac{1}{V} \int_{F_1^+} E_{11} x_1 \, dS - \frac{1}{V} \int_{F_1^-} E_{11} x_1 \, dS = E_{11} \qquad (C.2)$$

The spatial averages $\langle \varepsilon_{22} \rangle = E_{22}$ and $\langle \varepsilon_{33} \rangle = E_{33}$ are determined similarly. Let us now consider other components, for instance:

$$\langle \varepsilon_{12} \rangle = \frac{1}{V} \int_V \varepsilon_{12} \, dV = \frac{1}{V} \int_V u_{1,2} \, dV = \frac{1}{V} \int_{\partial V} u_1 n_2 \, dS$$

$$= \frac{1}{V} \left(\underbrace{\int_{F_1} u_1 n_2 \, dS}_{=0} + \int_{F_2} u_1 n_2 \, dS + \underbrace{\int_{F_3} u_1 n_2 \, dS}_{=0} \right) = \frac{1}{V} \left(\int_{F_2^+} u_1 \, dS - \int_{F_2^-} u_1 \, dS \right)$$

$$= \frac{1}{V} \left(\int_{F_2^+ \cap \partial V_f^{out}} u_1 \, dS + \int_{F_2^+ \cap \partial V_p^{out}} u_1 \, dS - \int_{F_2^- \cap \partial V_f^{out}} u_1 \, dS - \int_{F_2^- \cap \partial V_p^{out}} u_1 \, dS \right) \quad (C.3)$$

In our computations the surface integral over $\partial V_f^{out} \cap F_2$ can be evaluated. However, a suitable extrapolation of $\underline{u}$ on $\partial V_p^{out} \cap F_2$ is needed for the full evaluation of $\langle \varepsilon_{12} \rangle$. This holds for every component $\langle \varepsilon_{ij} \rangle \quad \forall i \neq j$.

Let us now consider the macroscopic stress field. From Eq. (28), it yields:

$$\Sigma_{ij} = V_V^f \langle \sigma_{ij} \rangle_f = \frac{1}{V} \int_{\partial V_f^{out}} \sigma_{(ik} n_k x_{j)} \, dS \qquad (C.4)$$

Each component of the stress field is considered:

$$\Sigma_{11} = V_V^f \langle \sigma_{11} \rangle_f \qquad (C.5)$$

In our computations, Σ_{11} is computed as a spatial average. Other components Σ_{ij} are computed in the same way:

$$\Sigma_{12} = \frac{1}{2V} \int_{\partial V_f^{out}} \sigma_{1k} n_k x_2 + \sigma_{2k} n_k x_1 \, dS$$

$$= \frac{1}{2V} \left(\int_{F_1} \left(\sigma_{11} n_1 x_2 + \underbrace{\sigma_{21} n_1 x_1}_{=0} \right) dS \right.$$

$$+ \int_{F_2} \left(\underbrace{\sigma_{12} n_2 x_2}_{=0} + \sigma_{22} n_2 x_1 \right) dS + \int_{F_3} \left(\underbrace{\sigma_{13} n_3 x_2}_{=0} + \underbrace{\sigma_{23} n_3 x_1}_{=0} \right) dS \right)$$

$$= \frac{1}{2V} \left(\int_{F_1} \sigma_{11} n_1 x_2 \, dS + \int_{F_2} \sigma_{22} n_2 x_1 \, dS \right)$$

$$(C.6)$$

which does not vanish in general.

C.2. Shear loading

Let us consider the spatial average of the strain using Eq. (C.1). If we now consider each component of the strain field, it yields:

$$\langle \varepsilon_{12} \rangle = \frac{1}{V} \int_V \varepsilon_{12} \, dV = \frac{1}{V} \int_V u_{1,2} \, dV = \frac{1}{V} \int_{\partial V} u_1 n_2 \, dS$$

$$= \frac{1}{V} \left(\underbrace{\int_{F_1} u_1 n_2 \, dS}_{=0} + \int_{F_2} u_1 n_2 \, dS + \underbrace{\int_{F_3} u_1 n_2 \, dS}_{=0} \right)$$

$$= \frac{1}{V} \int_{F_2} E_{12} x_1 n_2 \, dS$$

$$= \frac{1}{V} \int_{F_1^+} E_{12} \frac{L}{2} \, dS - \frac{1}{V} \int_{F_1^-} \left(-E_{12} \frac{L}{2} \right) dS = \frac{E_{12}}{V} L^3 = E_{12} \qquad (C.7)$$

Other components are now considered, for instance:

$$\langle \varepsilon_{11} \rangle = \frac{1}{V} \int_V \varepsilon_{11} \, dV = \frac{1}{V} \int_V u_{1,1} \, dV = \frac{1}{V} \int_{\partial V} u_1 n_1 \, dS$$

$$= \frac{1}{V} \left(\int_{F_1} u_1 n_1 \, dS + \underbrace{\int_{F_2} u_1 n_1 \, dS}_{=0} + \underbrace{\int_{F_3} u_1 n_1 \, dS}_{=0} \right)$$

$$= \frac{1}{V} \left(\int_{F_1^+} u_1 \, dS - \int_{F_1^-} u_1 \, dS \right)$$

$$= \frac{1}{V} \left(\int_{F_1 \cap \partial V_f^{out}} u_1 \, dS + \int_{F_1 \cap \partial V_p^{out}} u_1 \, dS \right) \qquad (C.8)$$

In our computations the surface integrals over $\partial V_f^{out} \cap F_1$ can be evaluated. However, a suitable extrapolation of $\underline{u}$ on $\partial V_p^{out} \cap F_1$ is needed for the full evaluation of $\langle \varepsilon_{11} \rangle$. This holds for every component $\langle \varepsilon_{ij} \rangle$.

From Eq. (C.4), the components Σ_{ij} are computed as spatial averages:

$$\Sigma_{12} = V_V^f \langle \sigma_{12} \rangle_f \tag{C.9}$$

For other components, it yields:

$$\Sigma_{11} = \frac{1}{V} \int_{\partial V_f^{out}} \sigma_{1k} n_k x_1 \, dS$$

$$= \frac{1}{V} \left(\underbrace{\int_{F_1} \sigma_{11} n_1 x_1 \, dS}_{=0} + \int_{F_2} \sigma_{12} n_2 x_1 \, dS + \underbrace{\int_{F_3} \sigma_{13} n_3 x_1 \, dS}_{=0} \right)$$

$$= \frac{1}{V} \int_{F_2} \sigma_{12} n_2 x_1 \, dS \tag{C.10}$$

which does not vanish in general.

References

Altendorf, H. 2011. 3D Morphological analysis and modeling of random fiber networks. Ph.D. thesis; MINES-ParisTech; Paris.

Amestoy, P.R., Duff, I.S., L'Excellent, J.Y., 2000. Multifrontal parallel distributed symmetric and unsymmetric solvers. Computer Methods in Applied Mechanics and Engineering 184, 501–520.

Auriault, J.L., 1991. Heterogeneous medium: is an equivalent macroscopic description possible? International Journal of Engineering Science 29 (7), 785–795.

Barbe, F., Decker, L., Jeulin, D., Cailletaud, G., 2001. Intergranular and intragranular behavior of polycrystalline aggregates. Part I: F.E. model. International Journal of Plasticity 17, 513–536.

Barbier, C., Dendievel, R., Rodney, D., 2009a. Numerical study of 3D-compressions of entangled materials. Computational Materials Science 45, 593–596.

Barbier, C., Dendievel, R., Rodney, D., 2009b. Role of friction in the mechanics of nonbounded fibrous materials. Physical Review E 80 (1), 016115.

Beran, M.J., 1968. Statistical Continuum Theories. Wiley.

Cailletaud, G., Forest, S., Jeulin, D., Feyel, F., Galliet, I., Mounoury, V., Quilici, S., 2003. Some elements of microstructural mechanics. Computational Materials Science 27, 351–374.

Chateau, C., Gélébart, L., Bornert, M., Crépin, J., Caldemaison, D., 2010. Multiscale approach of mechanical behaviour of sic/sic composites: elastic behaviour at the scale of the tow. Technische Mechanik 30 (1–3), 45–55.

Delisée, C., Jeulin, D., Michaud, F., 2001. Morphological characterization and porosity in 3D of cellulosic fibrous materials. Comptes-Rendus de l'Académie des Sciences – Serie IIb: Mécanique 329 (3), 179–185.

Dirrenberger, J., Forest, S., Jeulin, D., 2012. Elastoplasticity of auxetic materials. Computational Materials Science 64, 57–61.

Dirrenberger, J., Forest, S., Jeulin, D., 2013. Effective elastic properties of auxetic microstructures: anisotropy and structural applications. International Journal of Mechanics and Materials in Design 9 (1), 21–33.

Drugan, W.J., Willis, J.R., 1996. A micromechanics-based nonlocal constitutive equation and estimates of representative volume element size for elastic composites. Journal of the Mechanics and Physics of Solids 44 (4), 497–524.

Faessel, M., Jeulin, D., 2011. 3D multiscale vectorial simulations of random models. In: Proceedings of ICS13, 19–22 October 2011, Beijing.

Frey, P.J., 2001. YAMS: a fully automatic adaptive isotropic surface remeshing procedure. Technical Report 0252; INRIA; Domaine de Voluceau, Rocquencourt, BP 105, 78153 Le Chesnay Cedex, France.

Gélébart, L., Chateau, C., Bornert, M., 2009. Conditions aux limites mixtes normales. In: 19ème Congrès Français de Mécanique, 24–28 August 2009, Marseille.

Gitman, I.M., Askes, H., Sluys, L.J., 2007. Representative volume: existence and size determination. Engineering Fracture Mechanics 74, 2518–2534.

Glüge, R., Weber, M., Bertram, A., 2012. Comparison of spherical and cubical statistical volume elements with respect to convergence, anisotropy, and localization behavior. Computational Materials Science 63, 91–104.

Hashin, Z., 1983. Analysis of composite materials – a survey. Journal of Applied Mechanics 50, 481–505.

Hatami-Marbini, H., Picu, R.C., 2009. Heterogeneous long-range correlated deformation of semiflexible random fiber networks. Physical Review E 80 (4).

Hazanov, S., 1998. Hill condition and overall properties of composites. Archive of Applied Mechanics 68, 385–394.

Hazanov, S., Amieur, M., 1995. On overall properties of elastic heterogeneous bodies smaller than the representative volume. International Journal of Engineering Science 33 (9), 1289–1301.

Hazanov, S., Huet, C., 1994. Order relationships for boundary conditions effect in heterogeneous bodies smaller than the representative volume. Journal of the Mechanics and Physics of Solids 42 (12), 1995–2011.

Hill, R., 1963. Elastic properties of reinforced solids: some theoretical principles. Journal of the Mechanics and Physics of Solids 11, 357–372.

Huet, C., 1997. An integrated micromechanics and statistical continuum thermodynamics approach for studying the fracture behaviour of microcracked heterogeneous materials with delayed response. Engineering Fracture Mechanics 58 (5–6), 459–556.

Jean, A., Jeulin, D., Forest, S., Cantournet, S., N'Guyen, F., 2011. A multiscale microstructure model of carbon black distribution in rubber. Journal of Microscopy 241 (3), 243–260.

Jean, A., Willot, F., Cantournet, S., Forest, S., Jeulin, D., 2011. Large-scale computations of effective elastic properties of rubber with carbon black fillers. International Journal for Multiscale Computational Engineering 9 (3), 271–303.

Jeulin, D., 1991. Modèles de fonctions aléatoires multivariables. Sciences de la Terre 30, 225–256.

Jeulin, D., 2011. Variance scaling of Boolean random varieties. Technical Report; Centre de Morphologie Mathématique. N/10/11/MM (2011), hal-00618967, version 1.

Jeulin, D., 2012. Morphology and effective properties of multi-scale random sets: a review. Comptes-Rendus de l'Académie des Sciences – Serie IIb: Mécanique 340 (4–5), 219–229.

Kanit, T., Forest, S., Galliet, I., Mounoury, V., Jeulin, D., 2003. Determination of the size of the representative volume element for random composites: statistical and numerical approach. International Journal of Solids and Structures 40, 3647–3679.

Lantuéjoul, C., 1991. Ergodicity and integral range. Journal of Microscopy 161, 387–403.

Madi, K., Forest, S., Cordier, P., Boussuge, M., 2005. Numerical study of creep in two-phase aggregates with a large rheology contrast: implications for the lower mantle. Earth and Planetary Science Letters 237 (1–2), 223–238.

Matheron, G., 1971. The Theory of Regionalized Variables and its Applications. Les Cahiers du Centre de Morphologie Mathématique de Fontainebleau. Ecole des Mines de Paris.

Matheron, G., 1989. Estimating and Choosing. Springer-Verlag, Berlin.

Mezeix, L., Bouvet, C., Huez, J., Poquillon, D., 2009. Mechanical behavior of entangled fibers and entangled cross-linked fibers during compression. Journal of Materials Science 44 (14), 3652–3661.

Moulinec, H., Suquet, P., 1994. A fast numerical method for computing the linear and nonlinear mechanical properties of composites. Comptes-Rendus de l'Académie des Sciences – Serie IIb: Mécanique 318, 1417–1423.

Ostoja-Starzewski, M., 2002. Microstructural randomness versus representative volume element in thermomechanics. Journal of Applied Mechanics 69 (1), 25–35.

Oumarou, M., Jeulin, D., Renard, J., Castaing, P., 2012. Multi-scale statistical approach of the elastic and thermal behavior of a thermoplastic polyamid-glass fiber composite. Technische Mechanik 32 (2–5), 484–506.

Pahr, D.H., Zysset, P.K., 2008. Influence of boundary conditions on computed apparent elastic properties of cancellous bone. Biomechanics and Modeling in Mechanobiology 7, 463–476.

Pelissou, C., Baccou, J., Monerie, Y., Perales, F., 2009. Determination of the size of the representative volume element for random quasi-brittle composites. International Journal of Solids and Structures 46, 2842–2855.

Peyrega, C., Jeulin, D., Delisée, C., Malvestio, J., 2009. 3D morphological modelling of a random fibrous network. Image Analysis & Stereology 28, 129–141.

Picu, R.C., 2011. Mechanics of random fiber networks–a review. Soft Matter 7, 6768–6785.

Picu, R.C., Hatami-Marbini, H., 2010. Long-range correlations of elastic fields in semi-flexible fiber networks. Computational Mechanics 46, 635–640.

Poisson, S.D., 1837. Recherches sur la Probabilité des Jugements en Matière Criminelle et en Matière Civile. Bachelier, Paris.

Raghavan, P., 2002. DSCPACK: domain-separator codes for solving sparse linear systems. Technical Report CSE-02-004; Department of Computer Science and Engineering, The Pennsylvania State University; University Park, PA.

Sab, K., 1992. On the homogenization and the simulation of random materials. European Journal of Mechanics, A/Solids 11 (5), 585–607.

Sab, K., Nedjar, B., 2005. Periodization of random media and representative volume element size for linear composites. Comptes-Rendus de l'Académie des Sciences – Serie IIb: Mécanique 333, 187–195.

Salmi, M., Auslender, F., Bornert, M., Fogli, M., 2012. Apparent and effective mechanical properties of linear matrix-inclusion random composites: improved bounds for the effective behavior. International Journal of Solids and Structures 49, 1195–1211.

Schladitz, K., Peters, S., Reinel-Bitzer, D., Wiegmann, A., Ohser, J., 2006. Design of acoustic trim based on geometric modeling and flow simulation for non-woven. Computational Materials Science 38, 56–66.

Schroeder, W., Martin, K., Lorensen, B., 2006. The Visualization Toolkit: An Object-Oriented Approach To 3D Graphics, fourth ed. Kitware Inc. Publishers.

Serra, J., 1982. Image Analysis and Mathematical Morphology. Academic Press.

Shahsavari, A.S., Picu, R.C., 2013. Size effect on mechanical behavior of random fiber networks. International Journal of Solids and Structures 50, 3332–3338.

SIMULOG. 2003. TetMesh-GHS3D User's Manual; fourth ed.

Soare, M.A., Picu, R.C., 2007. An approach to solving mechanics problems for materials with multiscale self-similar microstructure. International Journal of Solids and Structures 44, 7877–7890.

Terada, K., Hori, M., Kyoya, T., Kikuchi, N., 2000. Simulation of the multi-scale convergence in computational homogenization approaches. International Journal of Solids and Structures 37, 2285–2311.